Interface-control technique of semiconductors for layered thin-film electronic devices

メタデータ	言語: English
	出版者:
	公開日: 2017-10-05
	キーワード (Ja):
	キーワード (En):
	作成者: 増田, 淳
	メールアドレス:
	所属:
URL	http://hdl.handle.net/2297/30570

Interface-control technique of semiconductors for layered thin-film electronic devices

増田　淳

平成8年1月

博士論文

Interface-control technique of semiconductors for layered thin-film electronic devices

金沢大学大学院自然科学研究科
物質科学専攻
材料物性講座

学　籍　番　号　93-2021
氏　　名　増田　淳
主任指導教官名　清水立生

Contents

Chapter 1 Introduction

1.1 Background of this study 1

1.2 Organization of this article 2

References in Chapter 1 5

Chapter 2 Experimental Procedures

2.1 Sample preparation

2.1.1 Preparation of MgO buffer layer by electron–beam evaporation 6

2.1.2 Preparation of MgO buffer layer and $Pb(Zr,Ti)O_3$ films by pulsed laser ablation 6

2.1.3 Plasma nitridation of GaAs 9

2.1.4 Plasma oxidation of Si 11

2.2 Sample characterization

2.2.1 X–ray photoelectron spectroscopy 12

2.2.2 Auger electron spectroscopy 16

2.2.3 X–ray diffraction 16

2.2.4 Scanning electron microscopy 18

2.2.5 Ellipsometry 18

2.2.6 Electron spin resonance 19

2.2.7 Electrical measurements of $Pb(Zr,Ti)O_3$ films 19

References in Chapter 2 20

Chapter 3 Preparation of Pb(Zr,Ti)O3 Films on Semiconductor Substrates
3.1 Background 21
3.2 MgO buffer layers prepared by electron-beam evaporation on GaAs and Si substrates 24
3.3 MgO buffer layers prepared by pulsed laser ablation on GaAs and Si substrates 32
3.4 Pb(Zr,Ti)O3 films prepared by pulsed laser ablation on GaAs substrates with MgO buffer layer 38
3.5 Pb(Zr,Ti)O3 films prepared by pulsed laser ablation on Si substrates with MgO buffer layer 43
3.6 Summary 47
References in Chapter 3 51

Chapter 4 Plasma Nitridation of GaAs
4.1 Background 54
4.2 Nitridation for various times and at various temperatures 58
4.3 Nitridation mechanism 67
4.4 Oxidation resistance of the nitrided layer 70
4.5 Excimer-laser irradiation on the nitrided layer 74
4.6 Summary 79
References in Chapter 4 80

Chapter 5 Plasma Oxidation of Si
5.1 Background 84
5.2 Oxidation process 85
5.3 N accumulation at the SiO2/Si interface 88
5.4 Oxide-growth mode 91
5.5 Electron spin resonance study on SiO2/Si interface 93
5.6 Summary 101
References in Chapter 5 102

Chapter 6 Conclusions 104

Acknowledgements 106

Publication Lists 108

Chapter 1 Introduction

1.1 *Background of this study*

Rapid progress of electronics in recent years is marvelous. Materials engineering is the most important elemental technique to support the electronics. For example, blue light emitting diodes (LEDs) using InGaN/GaN double-heterostructure developed by Nakamura *et al.* [1] is fresh in our memory. Quite recently they announced the success of laser oscillation in such Ⅲ – Ⅴ nitride material. Nonvolatile memories using ferroelectric materials have also been developed with a keen competition between private companies and universities. In recent years $SrBi_2Ta_2O_9$ of Bi-layer-structured ferroelectrics called Y1 is highly resistive against the fatigue with the polarization reversal [2]. The continuing scaling down of Si VLSIs and ULSIs has also been in progress. These progresses in device technology demand the more complicated fabrication processes including various integrations. Above all, interface control in the layered thin-film structure is one of the most important techniques for the integration. For example, newly developed electronic materials are often required to be integrated with Si or GaAs for the practical use because such conventional semiconductors are mainstream in electronic devices. Integration of new electronic materials and conventional semiconductors also pioneers the conception of new device structures. Therefore the integration of electronic materials recently attracting much attention, such as Ⅲ – Ⅴ nitride and ferroelectrics, with Si or GaAs is one of the key issues to be urgently solved.

This technique has, however, many difficult problems, such as lattice mismatch, interdiffusion and formation of the alloying layer at their interface. Formation of buffer layers between them is one of the most important techniques to solve these problems. Appropriate buffer layers act as the template layer for relaxing the lattice mismatch and also prevent both the interdiffusion and the formation of the alloying layer. Lattice constants and crystal structure for typical oxide ferroelectrics, candidates of oxide buffer layers are shown in Table 1.1 together with typical Ⅲ – Ⅴ nitrides, Si and GaAs. Ultrathin oxide films are also required for the scaling down of Si LSIs because of the scaling rule. Therefore severe thickness-control technique of ultrathin oxide films is also urgently required. In this case, SiO_2/Si interface-control technique is also important for controlling the oxide thickness.

1.2 *Organization of this article*

This article presents three examples of interface-control techniques using dry processes such as physical vapor deposition (PVD) and plasma modifications of semiconductors after systematically describing the experimental procedures in Chap. 2. Two examples are about the formation technique of buffer layers for ferroelectric films on GaAs and Si substrates shown in Chap. 3 and for GaN films on GaAs substrate shown in Chap. 4. The other example shown in Chap. 5 is about the plasma oxidation of Si for controlling both the ultrathin oxide thickness and SiO_2/Si interface at low temperature. Background, current topics and problems including device applications of these studies will be described in detail at the beginning of

Table 1.1 Lattice constants and crystal structure for typical oxide ferroelectrics and candidates of oxide buffer layers. Those for typical Ⅲ – Ⅴ nitrides, Si and GaAs are also shown.

Material	Crystal structure	Lattice constant (Å)
Ferroelectrics		
$BaTiO_3$	Perovskite	a=3.989, c=4.029
$PbTiO_3$	Perovskite	a=3.896, c=4.136
$Pb(Zr_{0.52}Ti_{0.48})O_3$	Perovskite	a=4.036, c=4.146
$LiNbO_3$	Similar to ilmenite	a=5.1494, c=13.8620
Candidates of buffer layer		
MgO	Rock salt	a=4.2112
CeO_2	Fluorite	a=5.409
$(ZrO_2)_{0.91}(Y_2O_3)_{0.09}$	Fluorite	a=5.185
TiO_2	Rutile	a=4.5929, c=2.9591
$SrTiO_3$	Perovskite	a=3.904
$SrRuO_3$	Perovskite	a=5.567, b=5.530, c=7.845
$MgAl_2O_4$	Spinel	a=8.086
Semiconductors		
GaN	Wurtzite	a=3.189, c=5.185
	Zinc-blende	a=4.52
InN	Wurtzite	a=3.548, c=5.760
	Zinc-blende	a=4.98
AlN	Wurtzite	a=3.112, c=4.982
	Zinc-blende	a=4.38
Si	Diamond	a=5.4309
GaAs	Zinc-blende	a=5.653

each chapter. Conclusions in this study will be summarized in Chap. 6.

References in Chapter 1

[1] S. Nakamura, M. Senoh and T. Mukai: Appl. Phys. Lett. **62** (1993) 2390.

[2] T. Mihara, H. Watanabe, C. A. Araujo, J. Cuchiaro, M. Scott, L. D. McMillan: *Proc. 4th Int. Symp. Integrated Ferroelectrics, Monterey, 1992*, p. 137.

Chapter 2 Experimental procedures

2.1 *Sample preparation*

2.1.1 *Preparation of MgO buffer layer by electron-beam evaporation*

MgO films were deposited by electron-beam (EB) evaporation for 40 min using sintered MgO targets of 99.9 % purity. Substrates used were *n*-type (100)Si and *n*-type (100)GaAs. The (100)Si substrates were cleaned with organic solvents followed by spin etching [1] with a 1:10:1 mixture of HF, C_2H_5OH and H_2O in N_2 ambient. Spin etching removes the native oxide and terminates the surface with H. The (100)GaAs substrates were also cleaned with organic solvents, etched in 10:1:1 solution of H_2SO_4, H_2O_2 and H_2O, and immersed in distilled water. The substrates were then spin-dried with ethanol in N_2 ambient. After the etching processes, the substrates were immediately introduced into the deposition chamber. The substrates were heated by a halogen lamp and substrate temperature was monitored with a thermocouple. The substrate temperature employed was between 280 ℃ and 610 ℃. The substrate-target distance was varied over the range from 11 cm to 16 cm. The electron-gun current was changed between 8 mA and 15 mA. The background pressure was the order of 10^{-3} Pa. The deposition rate was determined by the thickness measured using a surface profilometer.

2.1.2 *Preparation of MgO buffer layer and Pb(Zr,Ti)O3 films by pulsed laser ablation*

Both MgO buffer layers and Pb(Zr,Ti)O_3 (PZT) films were deposited by

the pulsed laser ablation (PLA) method. An ArF excimer laser, SHIBUYA ES5000, operating at a wavelength of 193 nm and at a pulse duration of 10 ns was used. Targets used for deposition of MgO layers were ceramic MgO pellets of the density of 98.9 % and of the purity of 99.9 %, or the metal Mg of the purity of 99.9999 %. Those for PZT films were sintered PZT pellets of a single perovskite phase with the composition of $Pb(Zr_{0.52}Ti_{0.48})O_3$ containing 1 wt.% Nb_2O_5. The laser fluence in this study was 7.0 J/cm^2 for MgO targets and 3.5 J/cm^2 for Mg targets. The repetition rate was fixed at 5 Hz for both MgO layers and PZT films. The distance between the target and the substrate was fixed at 35 mm. The schematic view of the apparatus is shown in Fig. 2.1. MgO buffer layers were deposited on (100)GaAs and (100)Si at the substrate temperatures ranging from 250 ℃ to 550 ℃. Substrates used were CrO-doped semi-insulating (100)GaAs with resistivity larger than 1.0×10^7 Ω•cm and *n*-type (100)Si with resistivity of the order of 10^{-2} Ω•cm. The (100)GaAs substrates were cleaned with an organic solvent, immersed in a 9:2:1 solution of H_2SO_4, H_2O_2 and H_2O, then rinsed in the distilled water. With this treatment, oxide layers on the surface were almost completely removed, which was confirmed by X-ray photoelectron spectroscopy (XPS) and will be in detail discussed in § 4.2. The (100)Si substrates were cleaned with an organic solvent, immersed in a 1:1:10 solution of HF, H_2O and C_2H_5OH, resulting in the H termination on the surfaces. After these wet-treatments, both substrates were dried by a N_2 blow and loaded into the chamber. The deposition of MgO was carried out in vacuum of the order of 10^{-5} Pa or in an O_2 ambient with pressures between 1.6×10^{-2} Pa and 1.3×10^2 Pa. PZT thin films were prepared at 510 ℃ in an O_2 ambient of 1.3×10^2 Pa, which was close to the optimized condition in the system used in this study [2].

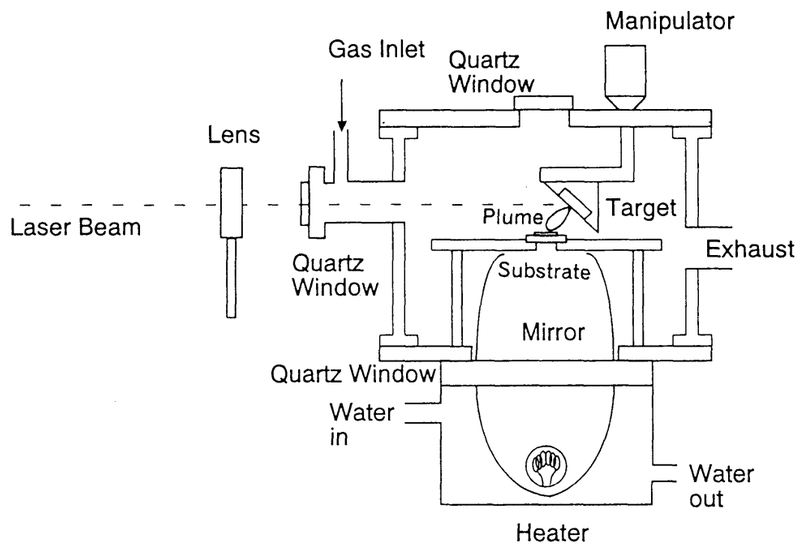

Fig. 2.1. Schematic view of the preparation chamber for the PLA of MgO buffer layer and PZT films.

2.1.3 *Plasma nitridation of GaAs*

CrO-doped semi-insulating (100), (111)A and (111)B GaAs substrates with resistivity greater than 1.0×10^{7} Ω •cm were employed in this study. The substrates were cleaned with organic solvents and immersed in a 9:2:1 solution of H_2SO_4, H_2O_2 and H_2O. Then, the substrates were rinsed in distilled water, dried in N_2 ambient and loaded into a stainless steel chamber. The background pressure of this chamber is about 4×10^{-5} Pa. Two parallel electrodes were set up with the distance of 33 mm. An rf voltage with the frequency of 13.56 MHz was applied to the cathode, and the substrates were placed on the anode which was grounded. A planar magnetic field was also applied parallel to the cathode in order to confine the plasma near the cathode and keep it away from the substrates to avoid plasma damage. After the required substrate temperature was attained, NH_3 gas of 99.999 % purity was introduced into the chamber. NH_3 plasma with a planar magnetic field was generated under the conditions of gas flow rate of 20 sccm, ambient pressure of 14 Pa and rf power density of 0.1 W/cm^{2}. The schematic view of the apparatus is shown in Fig. 2.2.

Two series of plasma treatments were carried out: one was performed fixing the treatment temperature at 250 ℃ and varying the treatment time over the range from 1 min to 60 min, and the other was performed fixing the treatment time at 20 min and varying the treatment temperature over the range from 50 ℃ to 300 ℃.

Some nitrided surfaces were irradiated by the ArF excimer laser of Shibuya ES5000 at room temperature (RT), 80 ℃ or 150 ℃ in the vacuum of the order of 10^{-5} Pa for 1 min. The wavelength, the laser fluence, the repetition frequency and the pulse duration were 193 nm, 30 mJ/cm^{2}, 10 Hz

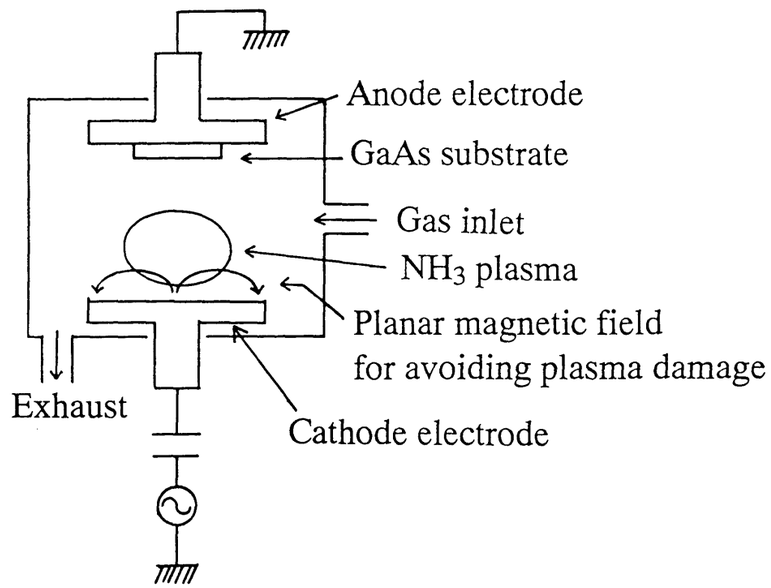

Fig. 2.2. Schematic view of the chamber for the plasma nitridation of GaAs.

and 10 ns, respectively.

2.1.4 *Plasma oxidation of Si*

The plasma oxidation was performed utilizing a conventional capacitively-coupled rf-plasma deposition system with a stainless-steel chamber. Substrates used in this study are three kinds of single-crystalline Si: *n*-type Czochralski (100)Si with the resistivity of 1×10^{-2} Ω•cm, *n*-type Czochralski (111)Si with that of 1×10^{-2} Ω•cm and *n*-type floating-zone-refined (111)Si with that of $1 \times 10^{3} - 5 \times 10^{3}$ Ω•cm. Samples for XPS measurements were formed on the low resistivity (100) and (111)Si substrates in order to avoid the charging. Those for electron spin resonance (ESR) measurements were formed on the high resistivity (111)Si substrates in order to avoid the microwave loss. All the substrates were cleaned with organic solvents, etched in 1:1:10 solution of HF, H_2O and C_2H_5OH, dried in N_2 ambient and immediately loaded into the chamber. It has been confirmed by XPS that there are almost no native oxide on the Si substrate surface after these aqueous treatments. Substrates were placed on the grounded anode electrode, and rf voltage with the frequency of 13.56 MHz was applied to the cathode electrode. The distance between electrodes and the cathode-electrode area were 43 mm and 81 cm^2, respectively. The chamber was once pumped down to a vacuum of the order of 10^{-5} Pa, and then the substrate was heated up to 300 ℃. The upper bound of substrate temperature is restricted to 300 ℃ in our apparatus although higher substrate temperature is supposed to bring about higher quality samples. However, lower substrate temperature is favorable to controlling the oxidation rate. After substrate temperature reached to 300 ℃, O_2 or N_2O gas of the purity of 99.999 % was introduced with the flow rate of 14 sccm and with the pressure

of 17 Pa. The plasma oxidation was performed with the rf power density of 0.15 W/cm ^{2}. The oxidation time was varied over the range from 1 min to 120 min. The schematic view of the apparatus is shown in Fig. 2.3.

2.2 *Sample characterization*

2.2.1 *X-ray photoelectron spectroscopy*

The apparatus employed for XPS measurements was an XPS-7000S spectrometer produced by Rigaku Industrial Co. The background pressure during measurements was less than 2×10^{-8} Pa. The X-ray source was Mg $K\alpha$ radiation of energy of 1253.6 eV with the voltage of 10 kV, the current of 20 mA and the pass energy of 15 eV unless otherwise noted. So-called angle-dependent XPS (ADXPS) measurements were performed with varying the photoelectron take-off angle, which was defined as the angle between the XPS detector and the sample surface, in the range between 90 deg and 20 deg. The depth profile of constituent elements for PZT/MgO/GaAs structure was also observed by XPS accompanied with Ar ion sputtering using monochromatic Al $K\alpha$ radiation of energy of 1486.6 eV with the voltage of 14 kV, the current of 100 mA and the pass energy of 15 eV. Ar ion sputtering was also carried out for observing the N depth profile for N_2O-plasma oxidized Si with Mg $K\alpha$ radiation because it is impossible to observe some samples with larger oxide thickness using ADXPS method as mentioned below. In both experiments Ar ion sputtering was carried out using the ion acceleration voltage of 500 V. It was also confirmed by comparison with the results from the ADXPS that the Ar ion sputtering in our experimental condition does not have a harmful effect on the resolution of the

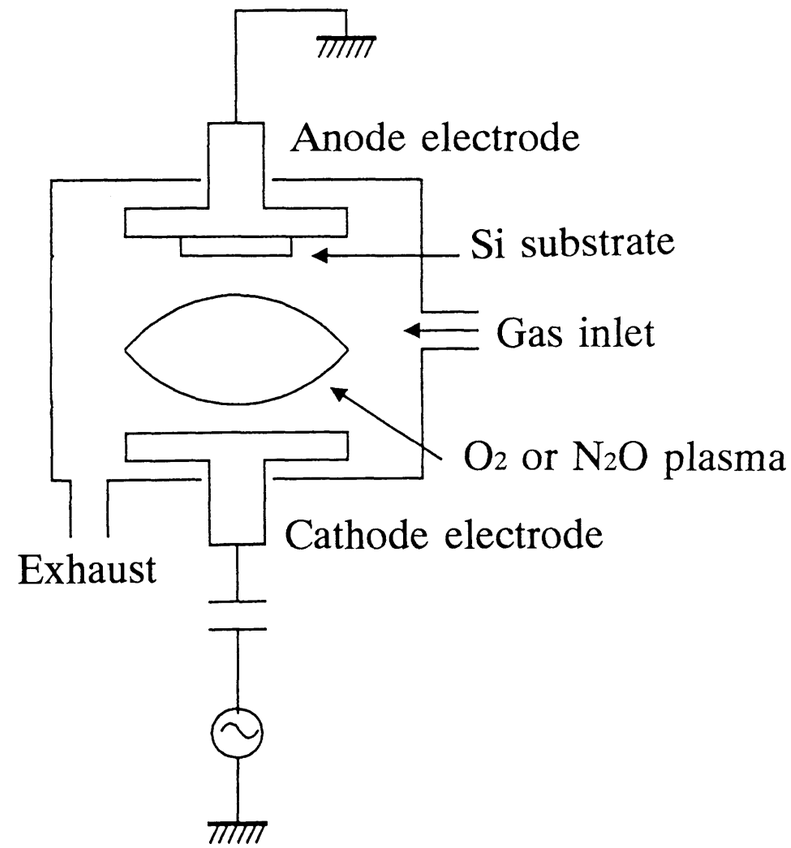

Fig. 2.3. Schematic view of the chamber for the plasma oxidation of Si.

depth profile.

The detailed surface reaction between GaAs surface and NH_3 plasma is analyzed by ADXPS. It is necessary for ADXPS analyses that the XPS signal due to the substrate is observed, namely film thickness is smaller than the photoelectron escape depth. Therefore the ADXPS is one of the powerful techniques for investigating the depth profile of the composition in ultrathin films without sample destruction [3]. Taking the photoelectron take-off angle of θ, as shown in Fig. 2.4, the XPS intensity $I(\theta)$ due to photoelectrons generated at the distance x from the surface is expressed by

$$I(\theta) \propto \exp\left(-\frac{x}{\lambda \sin\theta}\right), \qquad (2.1)$$

where λ is the electron escape depth. Normalized intensity using ADXPS analyses, $I_{norm}(\theta)$, is derived as follows. First, all the signal intensities at various θ are divided by the signal intensity of the bottom substrate at the same θ to cancel the effect due to the configuration of the XPS apparatus. Then, the divided values are normalized to 1.0 at θ of 90°. Therefore $I_{norm}(\theta)$ can be expressed by the following equation:

$$I_{norm}(\theta) = (I_1(\theta)/I_2(\theta))/(I_1(\theta=90\text{deg})/I_2(\theta=90\text{deg}))$$

$$= \exp\left(\frac{(x_2-x_1)(1/\sin\theta-1)}{\lambda}\right). \qquad (2.2)$$

Here, x_2 is the thickness of the ultrathin layer on the substrate, and x_1 is the distance between the sample surface and the position where the observed

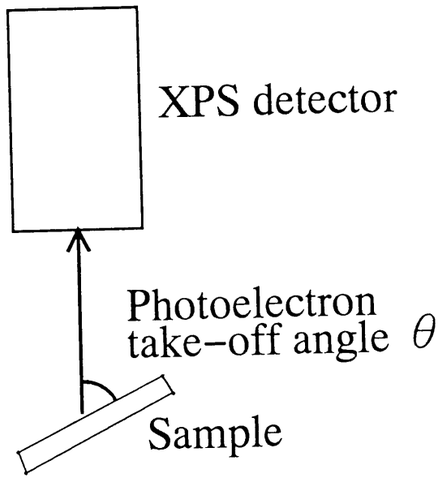

Fig. 2.4. Configuration of the XPS detector and the sample.

elements exist, as shown in Fig. 2.5. $I_2(\theta)$ and $I_1(\theta)$ are XPS intensities due to the substrate and elements in the ultrathin layer, respectively. Both x_1 and x_2 must be smaller than the photoelectron escape depth. It is clear from eq. (2.2) that $I_{norm}(\theta)$ is larger at smaller θ than that at larger θ when x_1 is smaller than x_2. On the other hand, $I_{norm}(\theta)$ is nearly equal to 1 regardless of θ when x_1 is nearly equal to x_2. Figure 2.6 shows the schematic θ dependence of $I_{norm}(\theta)$ for two regions.

In this study, the signal intensity of As 3*d* is adopted for that in GaAs substrate since the signal intensity of Ga 3*d* in GaAs has some ambiguity originating from the superposition of the signal from GaAs and that from the nitride in Ga 3*d* spectrum. In As 3*d* spectra, even when the signal due to As–N bonds is observed, the signal due to GaAs is separated more precisely because of the large difference in binding energies (BEs) between the signal due to GaAs and that due to As–N bonds.

2.2.2 *Auger electron spectroscopy*

The depth profile of constituent elements for PZT/MgO/Si structure was observed by Auger electron spectroscopy (AES) with Ar ion sputtering. The apparatus employed was JEOL JAMP-7100E. Acceleration voltage and diameter of electron beam were 10 kV and 1 μm, respectively. Ar ion sputtering was carried out with acceleration voltage of 2 kV. The sputtering rate was 60 Å /min in SiO_2 equivalent.

2.2.3 *X-ray diffraction*

The crystallinity of MgO and PZT films were characterized mainly using X-ray diffraction (XRD) with Cu $K\alpha$ radiation. Full-width at half maximum (FWHM) for θ -2 θ scan was estimated for observing the

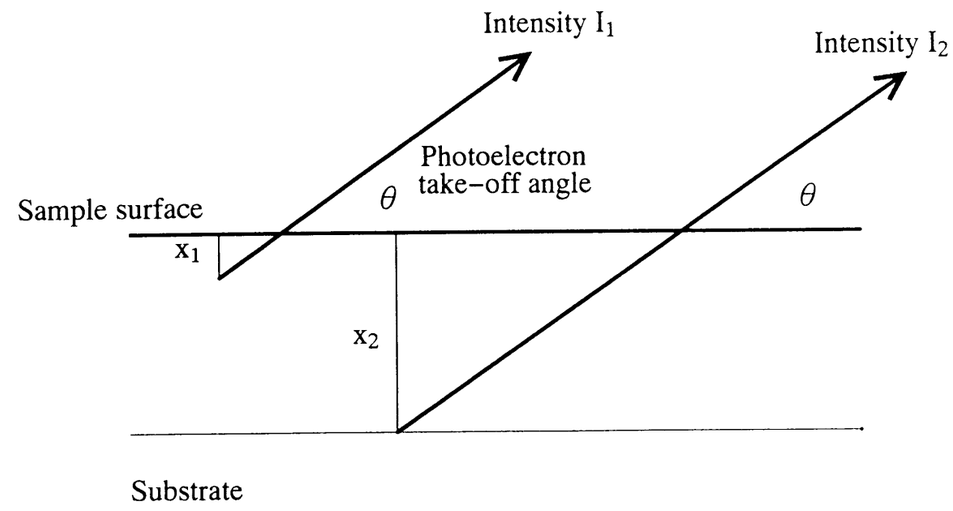

Fig. 2.5. Definition of XPS signal intensities of I_1 and I_2 due to the elements with the take-off angle of θ and with the distances from the surface of x_1 and x_2, respectively.

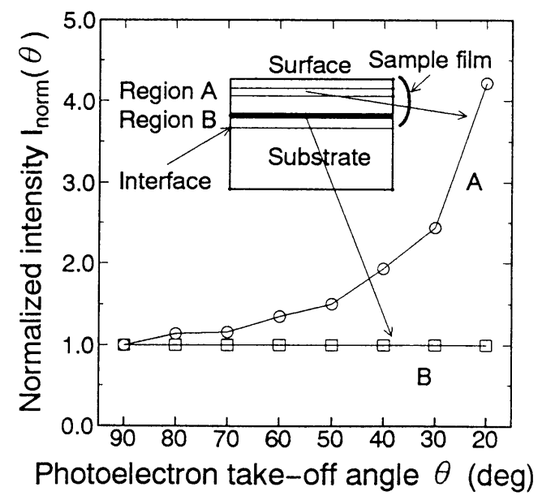

Fig. 2.6. Schematic θ dependence of $I_{norm}(\theta)$ for elements of films in two regions. Region A is near the surface and region B is near the interface between the sample film and the substrate.

number of grain boundaries, namely the grain size in the depth direction, and inhomogeneous strain in films. In addition to θ -2 θ scan, θ scan, often called rocking-curve measurement, was performed for estimating the misalignment of crystal plane parallel to the surface. ϕ -scan was also carried out for observing the in-plane orientation for MgO films prepared by EB evaporation. The apparatus employed for results shown in § 3.3 - 3.5 is Rigaku Industrial Co. RAD-rA. Acceleration voltage and current of X-ray radiation were 50 kV and 50 mA, respectively. Both divergence slit and scattering slit were fixed at 0.5 deg.

2.2.4 *Scanning electron microscopy*

Field-emission type scanning electron microscopy (FESEM) was utilized for inspecting the surface morphology and the crystallinity of MgO and PZT layers shown in § 3.3 - 3.5. The thickness of each layer was also estimated by SEM cross sectional images. The apparatus employed was Hitachi S-4000. Acceleration voltage and emission current were 10 kV and 10 μ A, respectively.

2.2.5 *Ellipsometry*

Ellipsometry using a He-Ne laser was employed for estimating the refractive indices of the MgO layer. SiO_2 thickness formed on Si substrate by the plasma-oxidation technique was also estimated using the ellipsometry with fixing the refractive index and the extinction coefficient for the oxide to 1.46 and 0.00, respectively. The results shown in § 3.3 and Chap. 5 were obtained using Mizojiri DVA-36L ellipsometer.

2.2.6 *Electron spin resonance*

ESR was observed for plasma-oxidized Si using JEOL JES RE-1X X-band spectrometer at RT.

2.2.7 *Electrical measurements of $Pb(Zr,Ti)O_3$ films*

Both the top electrode of Au on PZT films and the bottom electrode of Al on the back surface of Si were formed by evaporation at RT. Annealing at 400 ℃ in N_2 ambient was carried out for 20 min in order to obtain the ohmic contact after forming the Al electrode on the back surface of Si.

Sawyer-Tower circuit was used to observe the ferroelectric hysteresis for PZT films on Si with MgO buffer layer. The leakage current for PZT films was measured using YHP 4140B pA meter combined with a dc voltage source.

References in Chapter 2

[1] D. B. Fenner, D. K. Biegelsen and R. D. Bringans: J. Appl. Phys. **66** (1989) 419.

[2] H. Kidoh, T. Ogawa, A. Morimoto and T. Shimizu, Appl. Phys. Lett. **58** (1991) 2910.

[3] A. Masuda, I. Fukushi, Y. Yonezawa, T. Minamikawa, A. Morimoto, M. Kumeda and T. Shimizu: Jpn. J. Appl. Phys. **32** (1993) 2794.

Chapter 3 Preparation of $Pb(Zr,Ti)O_3$ Films on Semiconductor Substrates

3.1 *Background*

Ferroelectric thin films have attracted much attention because of various device applications of their ferroelectricity, high dielectric constant, piezoelectric, pyroelectric and electro-optical characteristics. Preparation of ferroelectric thin films with high quality on semiconductor substrates is a key issue for fabricating integrated devices composed of them. Following devices require the deposition of ferroelectric films on semiconductor substrates without electrodes. For example, photodeflectors using the acousto-optic effects, photomodulators using the electro-optic effects and laser diodes with short visible wavelength using quasi-phase-matching second-harmonic generation (QPM-SHG) will be realized as monolithic devices by integrating the optical waveguide of ferroelectric materials with the laser diode of compound semiconductors. Metal-ferroelectric-semiconductor field-effect transistors (MFS-FETs) proposed by Moll and Tarui [1] also need to prepare ferroelectric films on Si without electrodes. However, there have been few reports on the direct deposition of ferroelectric thin films on semiconductor substrates because of the large lattice mismatch between them and the alloying or the interdiffusion at their interface. Pb diffusion into the substrates was found for $(Pb,La)(Zr,Ti)O_3$ (PLZT) directly deposited on GaAs and GaP [2]. It was also reported that a SiO_2 layer is formed at the interface between PLZT and Si substrate [2]. Therefore buffer layers which not only relax the large

lattice mismatch but also act as a diffusion barrier should be employed.

There have been many reports on the heteroepitaxial growth of various oxide films on semiconductor substrates: CeO_2 on (100)Si [3] and on (100)GaAs [4], yttria-stabilized zirconia (YSZ) on (100)Si [5] and MgO on (100)Si [6] and on (100)GaAs [7]. Some of these oxide films were utilized for the buffer layer between semiconductors and oxide superconductors or oxide ferroelectric materials. It is required for the buffer layer not only to relax the lattice mismatch and to suppress the alloying at the interface but to suppress the vaporization of constituent elements from the substrate surface, if compound semiconductors such as GaAs are used for substrates. MgO films growing epitaxially on (100) GaAs and (100) Si at relatively low O_2 pressure and low temperature [6,7] are, in particular, promising candidates for the buffer layer because both low O_2 pressure and low temperature are suitable conditions to prevent oxide-layer formation on the substrate during the deposition of the buffer layer. The relatively lower O diffusion coefficient for MgO films as compared with CeO_2 films etc. [8] is appropriate for the buffer layer. MgO films prepared on GaAs at relatively low temperature are also expected to act as the diffusion barrier against the As-vaporization. Transmission electron microscopy (TEM) observation revealed the cube-on-cube epitaxy with four units of MgO and three units of GaAs in spite of a large lattice mismatch of 25.5 % between them [9]. Success in the orientation control of MgO films both on (100)Si and on (100)GaAs is also one of the important techniques to obtain the desired ferroelectric films on the buffer layer. This orientation control is in detail described in § 3.2. In the above-mentioned integrated optical devices composed of ferroelectric materials and compound semiconductors, the refractive index of MgO lower than that of most of ferroelectric materials also plays an important role in

confining the light from the laser diode of compound semiconductors within the optical waveguide of ferroelectric materials.

In recent years, there have been many reports on preparing epitaxial ferroelectrics on GaAs substrate with MgO buffer layer: $BaTiO_3$/MgO/(100)GaAs by pulsed laser ablation (PLA) [7,9,10], $PbTiO_3$/MgO/(100)GaAs by reactive rf magnetron sputtering [11] and $LiNbO_3$/MgO/(111)A or (111)B GaAs by PLA [12-14]. However, there has been no report on preparing Pb(Zr,Ti)O3 (PZT) films on GaAs substrate with MgO buffer layer because it is more difficult to prepare PZT films requiring higher growth temperature and higher O_2 pressure than $PbTiO_3$ films or $BaTiO_3$ films. The preparation of [100]-oriented perovskite PZT thin films by PLA on (100)GaAs with [100]-oriented MgO buffer layers is achieved in this study for the first time, as described in § 3.3.

The remarkable report was recently presented by Hirai *et al.* [15,16] with respect to preparing ferroelectrics on Si substrate with oxide buffer layer. They prepared $PbTiO_3$ films containing PbO_x phases on (100)Si substrate with CeO_2 buffer layer by metalorganic chemical vapor deposition (MOCVD) and examined the capacitance versus voltage (C-V) characteristics. Tokumitsu *et al.* [17,18] also reported the preparation of epitaxial PZT films on (100) and (111)Si with $SrTiO_3$ buffer layer. C-V characteristics of these films were also shown [18]. This article also reports the PLA preparation of [100]-oriented perovskite PZT films on (100)Si with [100]-oriented MgO buffer layers in § 3.4.

Here, the advantage of employing the PLA to prepare the multimetal-oxide thin films is also presented. PLA is the powerful method for preparing multielement-oxide thin films, such as $YBa_2Cu_3O_x$ (YBCO) [19,20], PZT [21,22] and Bi-substituted yttrium iron garnet (Bi:YIG) [23,24].

One reason is that it is easy to realize the stoichiometric deposition for multimetal–oxide films even if the target contains volatile elements with high vapor pressure such as Pb or Bi. The other one is that it is possible to deposit films in a high oxygen–pressure ambient because there is no energy source in the preparation chamber and because the PLA is a kind of the cluster deposition. Recently, it is clarified that both of them are closely related each other, namely the stoichiometric deposition of multimetal–oxide thin films containing volatile elements is realized only when the appropriate pressure of oxidant ambient is employed [25]. It is also available to change the target easily during the deposition for preparing the multilayer structure. Both the large–area deposition and reducing the droplet formation are inevitable issues to be solved for the industrial application of the PLA.

3.2 *MgO buffer layers prepared by electron-beam evaporation on GaAs and Si substrates*

In this section MgO films prepared by electron–beam (EB) evaporation will be discussed. Figure 3.1 shows the X–ray diffraction (XRD) θ –2 θ patterns with Cu $K\alpha$ radiation for the MgO films on (100)Si at various substrate temperatures with the electron–gun current I_{EG} of 20 mA and the target–to–substrate distance d_{ST} of 13 cm. Only (200) reflection due to [100] orientation and/or (111) reflection due to [111] orientation was observed for MgO films on (100)Si. Nearly [111] single orientation was observed at the substrate temperatures of 370 ℃ and 440 ℃, the mixture of [111] and [100] orientation was observed at 500 ℃, and [100] single orientation was observed at 610 ℃. Misalignment of the MgO crystal plane parallel to the surface was

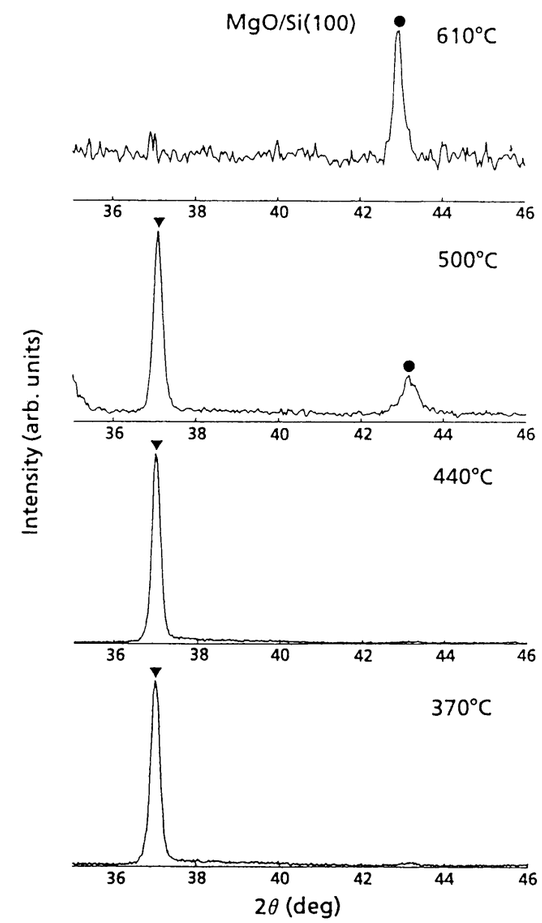

Fig. 3.1. XRD patterns of MgO films prepared on (100)Si at various substrate temperatures with I_{EG} of 20 mA and d_{ST} of 13 cm. Circular and triangular symbols show the diffraction due to (200)MgO and (111)MgO planes, respectively.

evaluated from the XRD rocking curve. The MgO films prepared at 370 ℃ with [111] orientation had a rocking curve full-width at half maximum (FWHM) of 6.81 ° . The rocking curve and ϕ scan of [100]-oriented MgO films were difficult to measure because of their thickness. The thickness of MgO films prepared on Si varied in the range from 0.1 μ m to 2.1 μ m because of a large change in the deposition rate. Figure 3.2 shows the substrate-temperature dependence of the [100]-orientation parameter p_{100} and the deposition rate for MgO films on (100)Si prepared at I_{EG} of 20 mA and d_{ST} of 13 cm. p_{100} was defined as

$$p_{100} = 0.1 \times I_{200} / (0.1 \times I_{200} + I_{111}), \qquad (3.1)$$

where I_{200} and I_{111} are the diffraction intensities of the (200) plane and (111) plane, respectively, and 0.1 is the relative intensity ratio of (111) to (200) according to the file of the Joint Committee on Powder Diffraction Standards (JCPDS). Figure 3.2 indicates a change in the orientation of MgO films from [111] to [100] with increasing the substrate temperature, accompanying a decrease in the deposition rate of MgO films. The deposition rate of the [111]-oriented MgO films was higher than 8.1 Å /s below 440 ℃ . While, the deposition rate of the [100]-oriented MgO films was 0.5 Å /s at 610 ℃ .

Although the MgO films prepared at 440 ℃ and I_{EG} of 20 mA had [111] preferred orientation, most MgO films prepared with I_{EG} of 8 mA had [100] single orientation regardless of d_{ST} from 11 cm to 16 cm. The deposition rate at I_{EG} of 20 mA was 9.8 Å /s, and that at I_{EG} of 8 mA was in the range from 0.1 Å /s to 0.3 Å /s independent of d_{ST}. The electron-gun-current dependence of p_{100} for MgO films prepared on (100)Si at 440 ℃ and d_{ST} of 13 cm is shown in Fig. 3.3. It is apparent that the

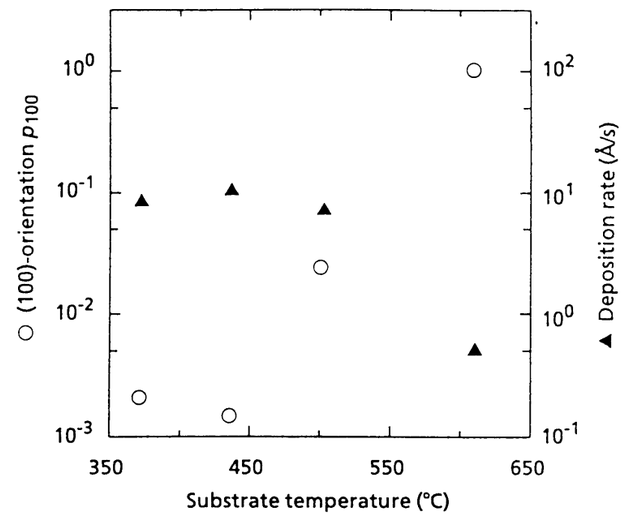

Fig. 3.2. [100]-orientation parameter and deposition rate of MgO films on (100)Si as a function of the substrate temperature at I_{EG} of 20 mA and d_{ST} of 13 cm.

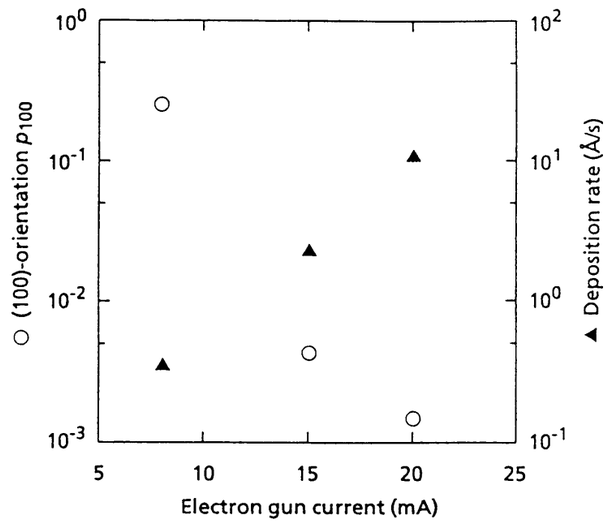

Fig. 3.3. [100]-orientation parameter and deposition rate of MgO films on (100)Si as a function of the electron-gun current at the substrate temperature of 440 ℃ and d_{ST} of 13 cm.

deposition rate become lower and p_{100} become larger at lower electron–gun current.

The observed relationship between the MgO orientation and the deposition rate is discussed in terms of the migration of molecules on a growing surface. At a low deposition rate, sufficient migration occurs to form the (100) plane of MgO which is energetically stable. The factors which contribute to lowering of the deposition rate are higher substrate temperature, lower electron–gun current or evaporation rate and longer target–to–substrate distance. The lower deposition rate due to higher substrate temperature results from decrease in the sticking coefficient of incoming molecules on the substrate, due to the desorption of molecules. The lower deposition rate due to both decreasing electron–gun current and increasing the target–to–substrate distance are caused by the smaller amount of molecules arriving on the growing surface. On the other hand, at a high deposition rate, insufficiently migration tends to form the energetically unstable (111) plane of MgO, which has lower atomic density than (100) plane.

On (100)GaAs substrates, MgO films were deposited at the substrate temperature from 280 ℃ to 500 ℃ with I_{EG} of 20 mA and d_{ST} of 13 cm. The deposited MgO films were between 0.3 μ m and 0.8 μ m in thickness. XRD patterns for MgO films prepared on (100)GaAs at various substrate temperatures at I_{EG} of 20 mA are shown in Fig. 3.4. Unlike the growth of MgO films on Si, MgO films had a strong tendency to develop [100] orientation on GaAs. MgO films had [100] single orientation above 370 ℃ and only MgO films prepared at 280 ℃ contained the (111) plane. The rocking curve FWHM of the (200)MgO peak for the sample prepared at 440 ℃ with I_{EG} of 20 mA was 0.90 ° . The resolution of the rocking curve scan measured on (200)GaAs was 0.53 ° . Tarsa *et al.* reported

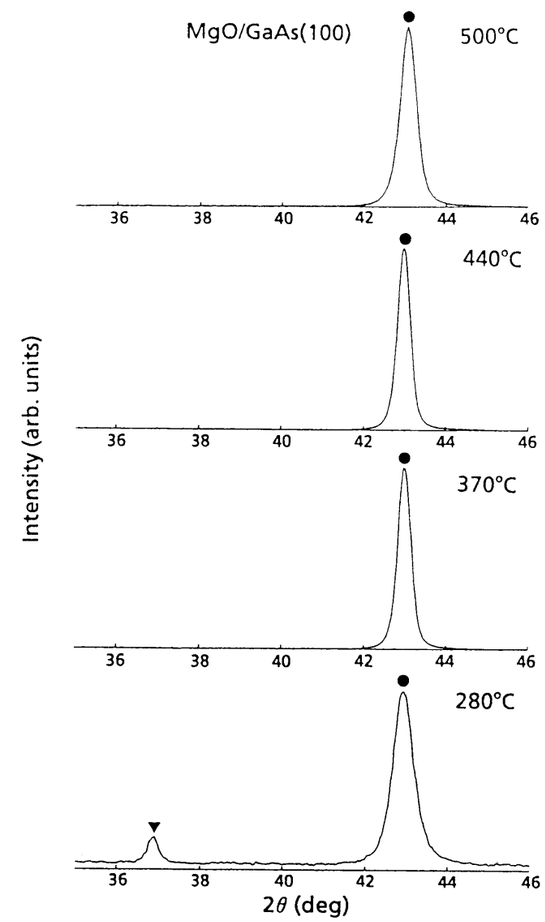

Fig. 3.4. XRD patterns of MgO films prepared on (100)GaAs at various substrate temperatures with I_{EG} of 20 mA and d_{ST} of 13 cm. Circular and triangular symbols show the diffraction due to (200)MgO and (111)MgO planes, respectively.

[111]-oriented MgO on partially oxide-desorbed (100)GaAs, polycrystalline MgO on oxide-desorbed (100)GaAs and [100]-oriented MgO on Sb-passivated (100)GaAs [26], whereas, [100]-oriented MgO films were obtained in this study above 370 ℃ without the surface-oxide sublimation process which was employed in the previous epitaxial growth of [100]-oriented MgO on (100)GaAs using the PLA [7,9,10]. The temperature of 370 ℃ is well below that required for sublimation of about 600 ℃ [27]. Considering these facts, the previously discussed deposition rate, which affects migration of molecules on a growing surface, is still the dominant factor governing the orientation of MgO films on (100)GaAs.

It was observed that MgO films had [100] single orientation even at 280 ℃ when I_{EG} was decreased to 8 mA. The deposition rate was 1.4 Å /s under this condition and 2.2 Å /s at 280 ℃ with I_{EG} of 20 mA, showing that the deposition rate has an effect on the orientation of MgO. The rocking curve FWHM of (200)MgO was still 1.67 ° although the MgO films were grown at a fairly low temperature. In-plane orientation of MgO films have been verified by off-axis XRD ϕ scans, which are similar measurements as the XRD pole figure method, using the (202)MgO and (202)GaAs reflections with the ϕ axis normal to the plane of (100)GaAs, as reported by Fork *et al.* [6]. The ϕ scan showed (202)MgO peaks at the interval of 90 ° with the same rotation angles as those of (202)GaAs. Part of XRD ϕ scan pattern is shown in Fig. 3.5 [28]. This result indicates the cube-on-cube epitaxy, that is, [001]MgO ‖ [001]GaAs. The refractive index, measured by the ellipsometry using a He-Ne laser, of this MgO film was 1.72, which is close to that of the single-crystalline bulk MgO, namely 1.702 [29]. Figure 3.6 shows a cross-sectional scanning electron microscopy (SEM) image of a (100)MgO/(100)GaAs heteroepitaxial structure prepared under this condition.

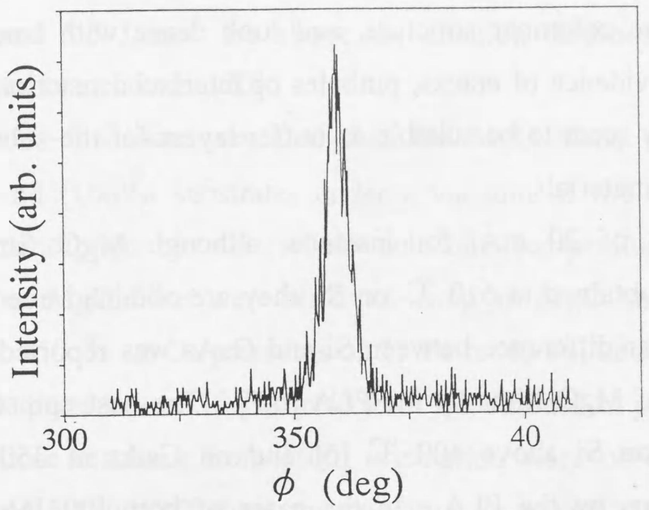

Fig. 3.5. XRD ϕ -scan patterns of MgO films prepared on (100)GaAs at 280 ℃ with I_{EG} of 8 mA and d_{ST} of 13 cm [28].

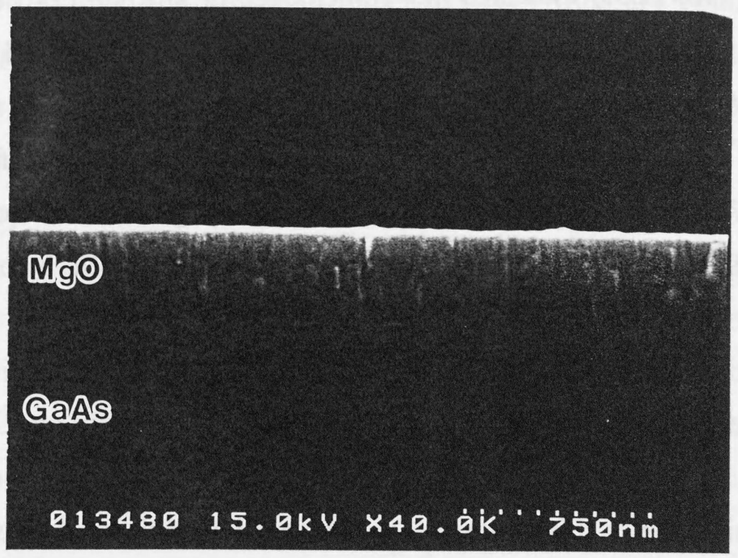

Fig. 3.6. Cross-sectional SEM image of the cleaved plane of (100)MgO/(100)GaAs heteroepitaxial structure prepared at 280 ℃ with I_{EG} of 8 mA and d_{ST} of 13 cm.

MgO films have columnar structure, and look dense with smooth surface. There was no evidence of cracks, pinholes or interfacial reactions. MgO films with this quality seem to be suitable as buffer layers for the subsequent growth of ferroelectric materials.

With ÆG of 20 mA, for instance, although MgO films with [100] orientation are obtained at 610 ℃ on Si, they are obtained even at 370 ℃ on GaAs. A similar difference between Si and GaAs was reported in the case of the deposition of MgO films by the PLA [6,7]. The best epitaxial MgO films were obtained on Si above 400 ℃ [6] and on GaAs at 350 ℃ [7] under similar conditions by the PLA. In the cases of both [001]MgO || [001]Si and [001]MgO || [001]GaAs, the lattice mismatch between MgO and Si is 22.2 % and between MgO and GaAs is 25.5 %, whereas, the previous lattice images observed by cross-sectional high-resolution transmission electron microscopy (HRTEM) indicated 4:3 coincidence of site lattices between MgO and GaAs [9,10]. When 4:3 lattice matching is considered, the lattice mismatch between MgO and Si is 3.4 % and that between MgO and GaAs is 0.7 %. This difference in lattice matching could have influenced the low-temperature formation of [100]-oriented MgO films on GaAs as compared with that on Si.

3.3 *MgO buffer layers prepared by pulsed laser ablation on GaAs and Si substrates*

In this section MgO films prepared by the PLA will be discussed. During the deposition of MgO buffer layers a bright green plume was observed in a direction normal to the target, showing that the laser fluences of

7.0 J/cm^2 and 3.5 J/cm^2 are above the ablation threshold for MgO target and Mg target, respectively [30].

XRD θ -2 θ scan revealed that the MgO films deposited on both (100)GaAs and (100)Si substrates under a vacuum of the order of 10^{-5} Pa are almost amorphous in the whole substrate temperature investigated. [100]-oriented MgO films were obtained using an MgO target on (100)GaAs at 400 ℃ or 450 ℃ at O2 pressures of 13 Pa or 40 Pa, and also on (100)Si at 450 ℃ at O2 pressures of 13 Pa or 40 Pa. No diffraction peaks due to planes other than those resulting from [100] orientation were observed. Large and small symbols in Fig. 3.7 show the condition in which [100]-oriented MgO films are obtained and the condition in which MgO films showing no diffraction peaks are obtained, respectively. Circles and triangles represent samples on GaAs substrate and on Si substrate, respectively. Figure 3.7 shows that the region where [100]-oriented MgO films are obtained is not so broad. The reason why only [100]-oriented MgO films were obtained by the PLA under the conditions in this study can be explained by the low deposition rate ranging from 0.4 Å /s to 2.2 Å /s, as discussed in § 3.2 for films prepared by the EB evaporation. Also in the PLA shown in this study, [100]-oriented MgO films were obtained at lower substrate temperature on (100)GaAs than on (100)Si, as shown in Fig. 3.7. XRD patterns for a series of MgO films deposited on (100)Si at 450 ℃ with various conditions are shown in Fig. 3.8. In the present study, the substrate temperature was elevated under the vacuum of the order of 10^{-5} Pa. The O2 gas was normally introduced into the preparation chamber with a delay time of 30 s or 1 min after the deposition of MgO films had started. This is because, as shown in Fig. 3.8 (c), the introduction of O2 gas just before the deposition yields amorphous MgO layers. This finding suggests that O2 gas introduced

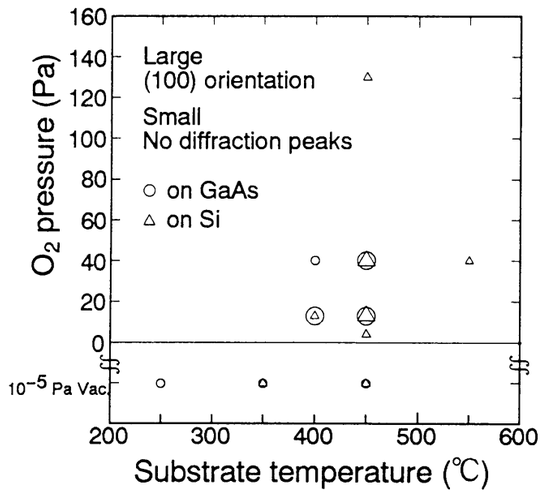

Fig. 3.7. Crystallinity of MgO films prepared on GaAs substrate (circles) and on Si substrate (triangles) is plotted in the graph showing the preparation conditions. Large symbols show the condition in which [100]-oriented MgO films are obtained and small ones show that in which MgO films showing no diffraction peaks are obtained.

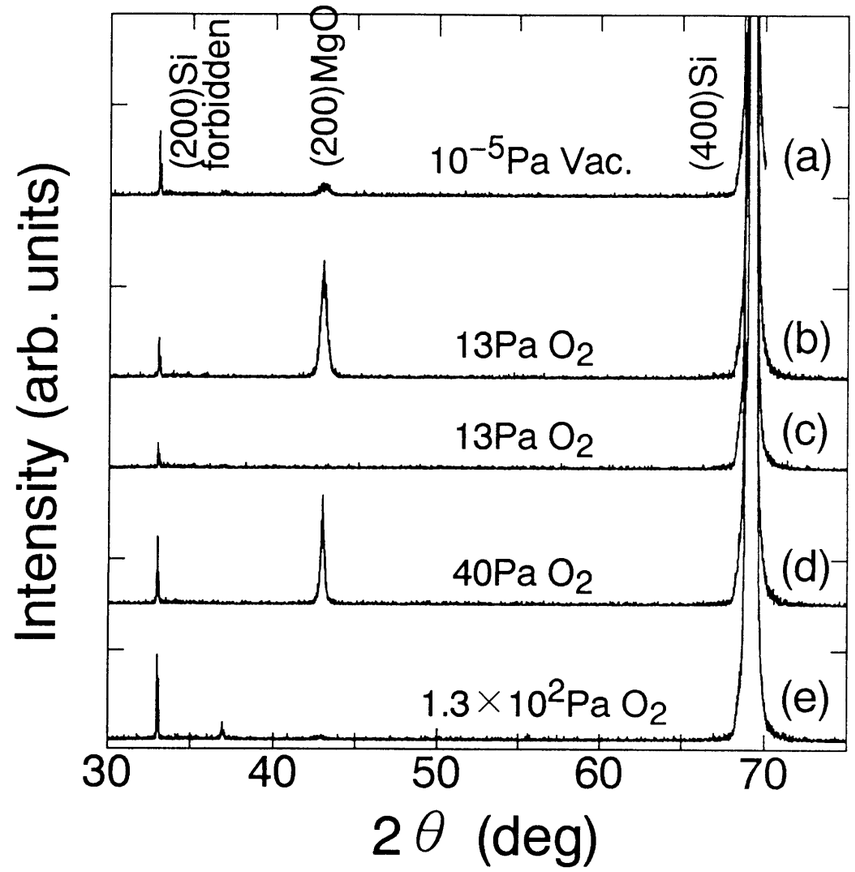

Fig. 3.8. XRD patterns for MgO films deposited on (100)Si at 450 ℃ using an MgO target (a) under the vacuum of the order of 10^{-5} Pa, (b) with O_2 pressure of 13 Pa, (d) with that of 40 Pa and (e) with that of 1.3×10^{2} Pa. O_2 gas was introduced after the deposition for 1 min for samples shown in (a), (b), (d) and (e). XRD pattern shown in (c) is for MgO films prepared with the same condition as those shown in (b), except that O_2 gas was introduced from the beginning of the deposition.

before the deposition of MgO films forms an oxide layer on the substrate, which leads to the degradation of the crystallinity of MgO films, and that the predeposition layer for only 1 min acts as an oxidation barrier during the deposition of MgO layer following the predeposition. Hereafter only results obtained for the sample subjected to the 1-min predeposition of the MgO layer will be presented unless otherwise noted.

The refractive indices of [100]-oriented MgO films both on (100) GaAs and (100) Si, estimated by ellipsometry using a He-Ne laser, are between 1.6 and 1.7, showing that the refractive indices of MgO films prepared in this study are similar to that of the single-crystalline bulk MgO, namely 1.702 [29], in the same way as MgO films prepared by the EB evaporation described in § 3.2.

[100]-oriented MgO films were also obtained using Mg target on (100)GaAs at 400 ℃ even at an O_2 pressure of 4 Pa. This result, combined with the results in the literature[6,7,9,10,12-14] suggests that in preparing high-quality MgO films PLA using a ceramic MgO target requires higher pressure of O_2 ambient than PLA using a metal Mg target. It is probable that the heat generated by the oxidation of Mg species during the transport assist the crystallization of MgO, resulting in the formation of high quality MgO films in lower O_2 pressures by PLA using an Mg target, as compared with PLA using an MgO target. Tiwari et al. [31] reported that [111]-oriented MgO films were obtained on (100)Si by PLA using a ceramic MgO target, differently from this case. In their report the O_2 pressure was not clearly shown.

The cross-sectional field-emission type SEM (FESEM) images of MgO/(100)GaAs prepared at 400 ℃ using MgO and Mg targets are shown in Figs. 3.9 (a) and (b), respectively. The ambients during the deposition were

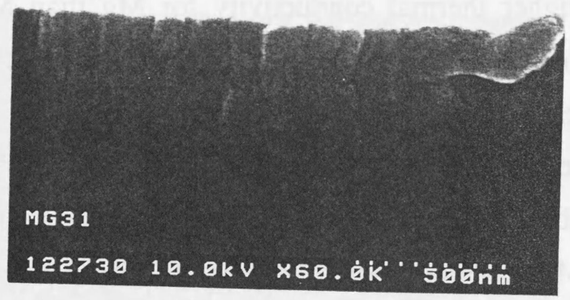

(a)

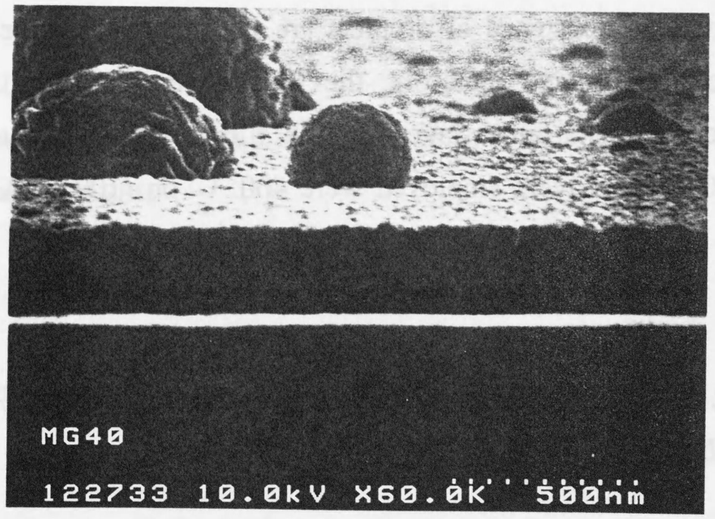

(b)

Fig. 3.9. Cross-sectional FESEM images of MgO/(100)GaAs prepared at 400 ℃ using (a) an MgO target and (b) an Mg target.

(a) O_2 of 13 Pa and (b) O_2 of 4 Pa. Figure 3.9 suggests that the PLA using an Mg target at a laser fluence of 3.5 J/cm^2 causes many droplets on the surface in contrast to the case of an MgO target at laser fluence of 7.0 J/cm^2, although it is known that higher laser fluence creates a larger number of droplets [32]. Higher thermal conductivity for Mg than MgO is possible to cause larger amount of ejected droplets for the PLA of Mg although the absorption coefficient for the ArF excimer laser is higher for Mg than MgO. This idea is supported by the fact that the etching depth after the ablation for an Mg target is about twice as large as that for an MgO target. On the other hand, the FESEM image, shown in Fig. 3.10, of MgO films deposited on (100)GaAs using an MgO target at 400 ℃ in O_2 ambient of 13 Pa exhibits a relatively flat surface composed of small crystallites without droplets. For device applications, especially for fabricating optical devices, the surface roughness and the existence of droplets are not suitable for the underlayer of ferroelectric thin films. Therefore, the MgO layer prepared using an MgO target was chosen as a buffer layer for PZT films. The substrate temperatures for the MgO buffer layers employed were 400 ℃ on (100)GaAs and 450 ℃ on (100)Si, respectively, at a fixed O_2 pressure of 13 Pa.

3.4 *$Pb(Zr,Ti)O_3$ films prepared by pulsed laser ablation on GaAs substrates with MgO buffer layer*

PZT films were deposited by the PLA on the [100]-oriented MgO buffer layers on (100)GaAs described in § 3.3. Figure 3.11 shows the XRD pattern obtained by the θ -2 θ scan for PZT films with the thickness of 1.0 μ m on (100)GaAs with [100]-oriented MgO buffer layer of 0.2 μ m.

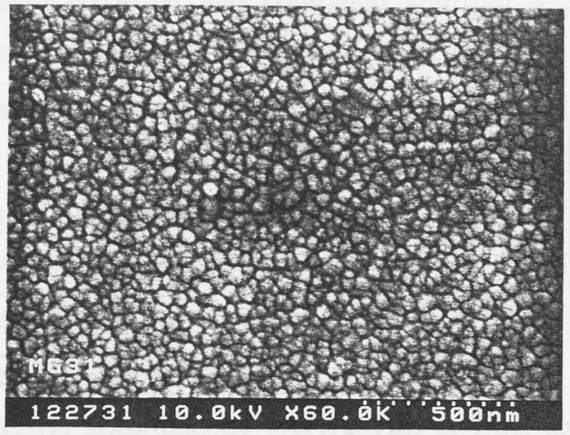

Fig. 3.10. Surface morphology of MgO films deposited on (100) GaAs at 400 ℃ in O_2 ambient of 13 Pa inspected by FESEM.

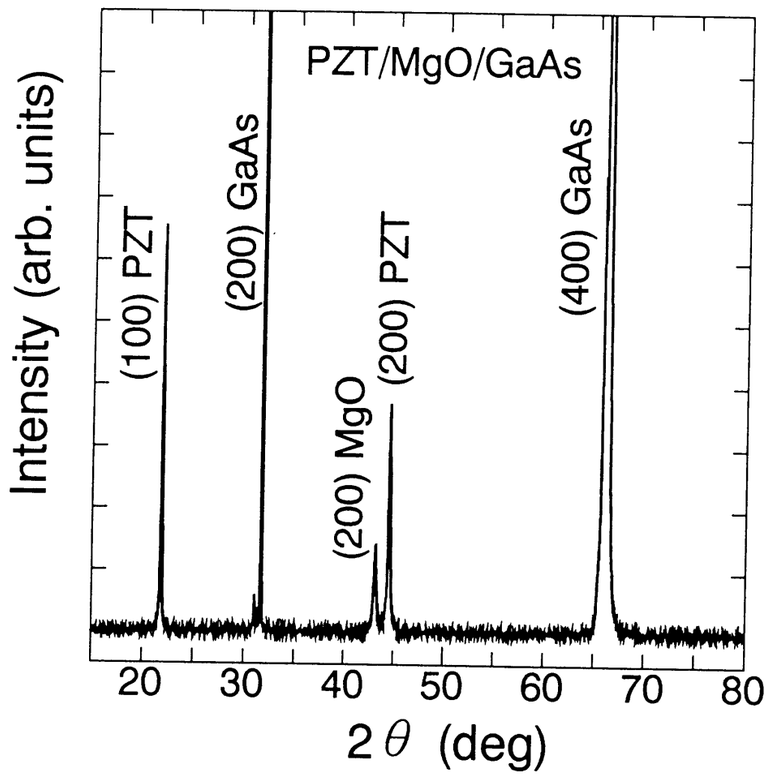

Fig. 3.11. XRD pattern for PZT films on (100) GaAs substrate with MgO buffer layer of 0.2 μm thickness.

Diffraction lines originating only from the (100) and (200) perovskite PZT planes are observed at 2 θ of 21.8 deg and 44.6 deg, respectively, in addition to those due to (200)MgO plane and GaAs substrates. The ratio of the FWHM for (200) PZT diffraction signal to that for (100) PZT diffraction signal, $FWHM_{200}/FWHM_{100}$, was compared with $\tan\theta_{200}/\tan\theta_{100}$ and $\cos\theta_{100}/\cos\theta_{200}$, where θ_{100} and θ_{200} are the peak angles of (100) and (200) PZT diffractions, respectively. As a result, $FWHM_{200}/FWHM_{100}$ was nearly equal to $\tan\theta_{200}/\tan\theta_{100}$; however, $FWHM_{200}/FWHM_{100}$ was much larger than $\cos\theta_{100}/\cos\theta_{200}$, indicating the existence of inhomogeneous strain in this structure [33].

The depth profile of constituent elements of the PZT/MgO/GaAs structure whose XRD pattern was shown in Fig. 3.11 was observed using X-ray photoelectron spectroscopy (XPS) with Ar ion sputtering as shown in Fig. 3.12. Ar ion sputtering was carried out at the acceleration voltage of 500 V and for 60 s per cycle. It was confirmed that both the compositions of PZT films and of GaAs surface estimated by XPS without sputtering are almost stoichiometric. Therefore the deviation of the compositions of both PZT films and GaAs substrate in Fig. 3.12 is supposed to originate from the preferential sputtering. Although detailed and precise discussion is difficult because there is the preferential sputtering and XPS observes a wide area sputtered without abruptness, neither fatal interdiffusion nor fatal formation of alloyed layer is found from Fig. 3.12 both at PZT/MgO and at MgO/GaAs interfaces. This fact implies that the MgO buffer layer acts as a barrier against the oxidation of GaAs and against the diffusion of Pb into GaAs, and also as a capping layer against vaporization of As from GaAs even under the severe conditions of high substrate temperature and high O_2 pressure for preparing PZT films. It was also confirmed from the cross-sectional FESEM image that PZT films

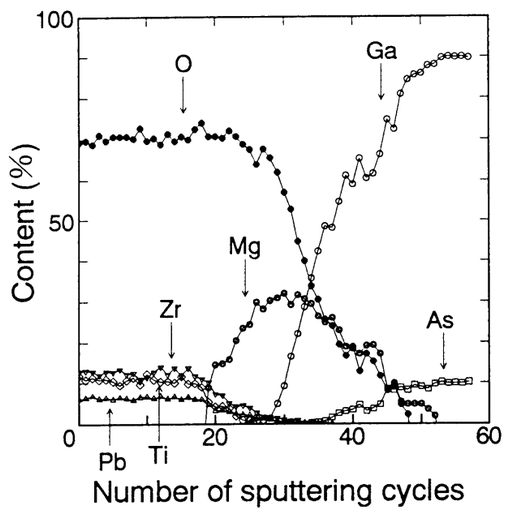

Fig. 3.12. Depth profile of constituent elements of the PZT/MgO/GaAs structure observed using XPS with Ar ion sputtering. The deviation of the compositions of both the PZT films and the GaAs substrate is supposed to originate from the preferential sputtering.

have a columnar structure.

3.5 *Pb(Zr,Ti)O3 films prepared by pulsed laser ablation on Si substrates with MgO buffer layer*

PZT films were also deposited by the PLA on the [100]-oriented MgO buffer layers on (100)Si described in § 3.3. Highly [100]-oriented PZT films with the thickness of 1.0 μ m consisting of only the perovskite phase were also obtained on (100)Si substrate with MgO buffer layer of 0.4 μ m thickness. However, in the layered structure with sandwich-type electrode, the voltage applied is divided in inverse proportion to the dielectric constant of each layer. Therefore in order to apply the PZT/MgO/Si structure to MFS-FETs, it is necessary to decrease the MgO-layer thickness because of the low dielectric constant of 9.8 for MgO at room temperature (RT). Figure 3.13 shows the XRD patterns obtained by the θ -2 θ scan for PZT films on (100)Si with MgO buffer layers of various thicknesses. As shown in Fig. 3.13 (a), PZT films directly deposited on (100)Si without MgO buffer layer exhibit only the pyrochlore phase. PZT films deposited on (100)Si with MgO buffer layer of 25 Å thickness exhibit also the diffraction peaks mainly due to the pyrochlore phase, although those due to a perovskite phase with a random orientation can also be seen, as shown in Fig. 3.13 (b). However, it is found from Fig. 3.13 (c) that [100]-oriented perovskite-phase PZT films can be obtained on (100)Si with MgO buffer layer of only 50 Å thickness, although the diffraction peaks of a small intensity due to the pyrochlore phase can also be observed. [100]-oriented PZT films consisting of only the perovskite phase grow on (100)Si with MgO buffer layer of 100 Å thickness,

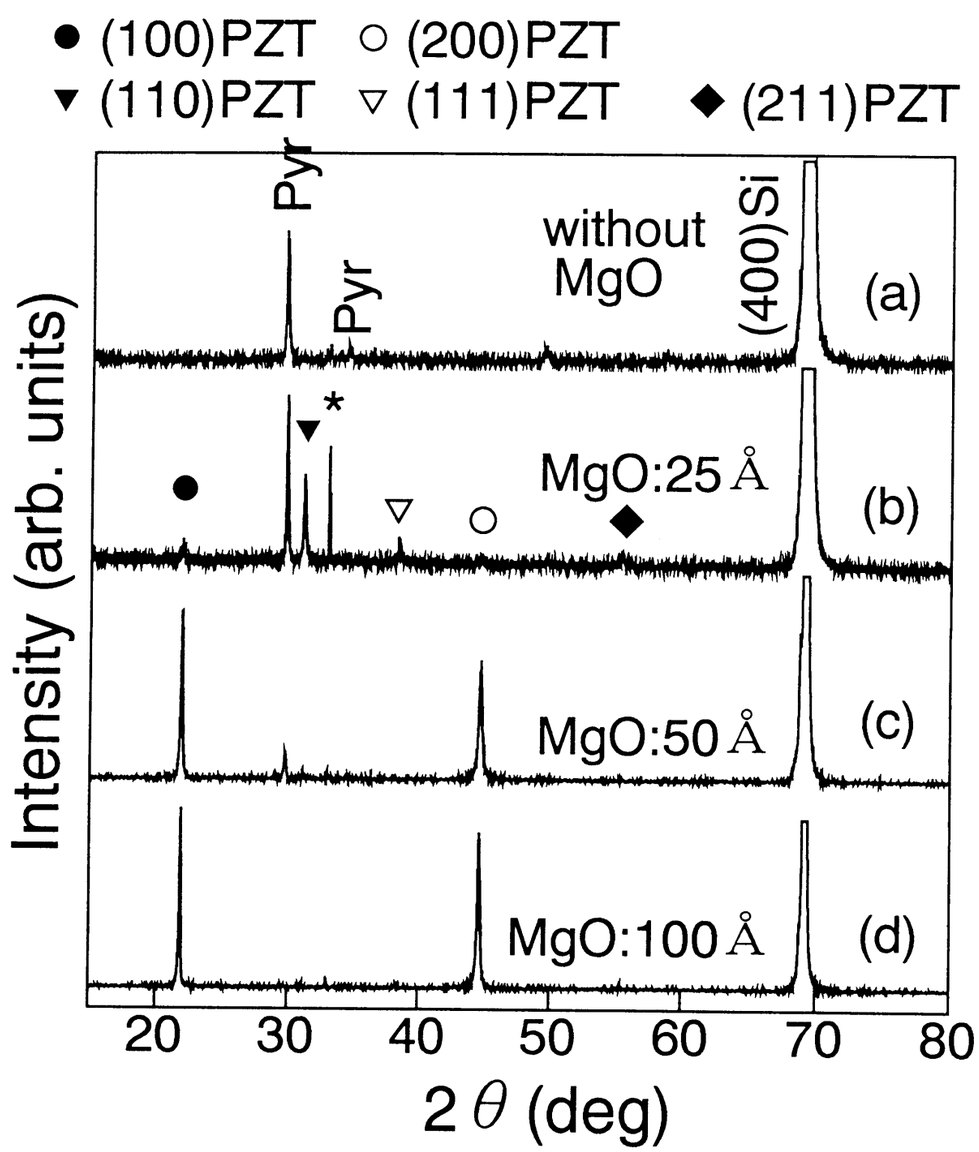

Fig. 3.13. XRD patterns for PZT films on (100)Si substrate with MgO buffer layers of various thicknesses. The peak marked by an asterisk in (b) is the (200)Si forbidden line.

as shown in Fig. 3.13 (d). In these cases the MgO–layer thickness was estimated from the deposition rate. The predeposition times for 25– and 50–Å –thick MgO buffer layers were 15 s and 30 s, respectively, because their total deposition times were 30 s and 1 min. The diffraction due to the (200)MgO plane is hardly seen because of the small thickness of the MgO layer. These results suggest the remarkable effects of the MgO buffer layer on the growth of highly oriented perovskite–phase PZT films. Namely, the MgO buffer layer is highly resistant against the degradation of Si substrates even under the conditions of higher substrate temperatures and higher O_2 pressures for the deposition of high quality PZT films than those for the deposition of MgO films. This finding is supported by also the depth profile of constituent elements observed using Auger electron spectroscopy (AES). The depth profile for PZT/Si structure without MgO buffer layer is shown in Fig. 3.14 (a). Interdiffusion between PZT layer and Si substrate is observed. For PZT/MgO/Si structure with MgO layer of 50 Å thickness, on the other hand, no interdiffusion between PZT layer and Si substrate is observed, as shown in Fig. 3.14 (b). This fact suggests that MgO layer with the thickness of only 50 Å acts as the diffusion barrier between PZT layer and Si substrate. It is possible that the crystallites of MgO initiate the growth of PZT films with the perovskite phase. However, it is supposed that MgO buffer layer of 25 Å thickness does not act as a diffusion barrier between PZT films and Si substrate.

Inhomogeneous strain was also found in all the [100]–oriented perovskite–phase PZT films deposited on (100)Si irrespective of MgO–buffer–layer thickness, similar to those deposited on (100)GaAs with MgO buffer layer. The surface morphology and the cross–sectional images observed by FESEM for the PZT/MgO/(100)Si structure consisting of a 0.1

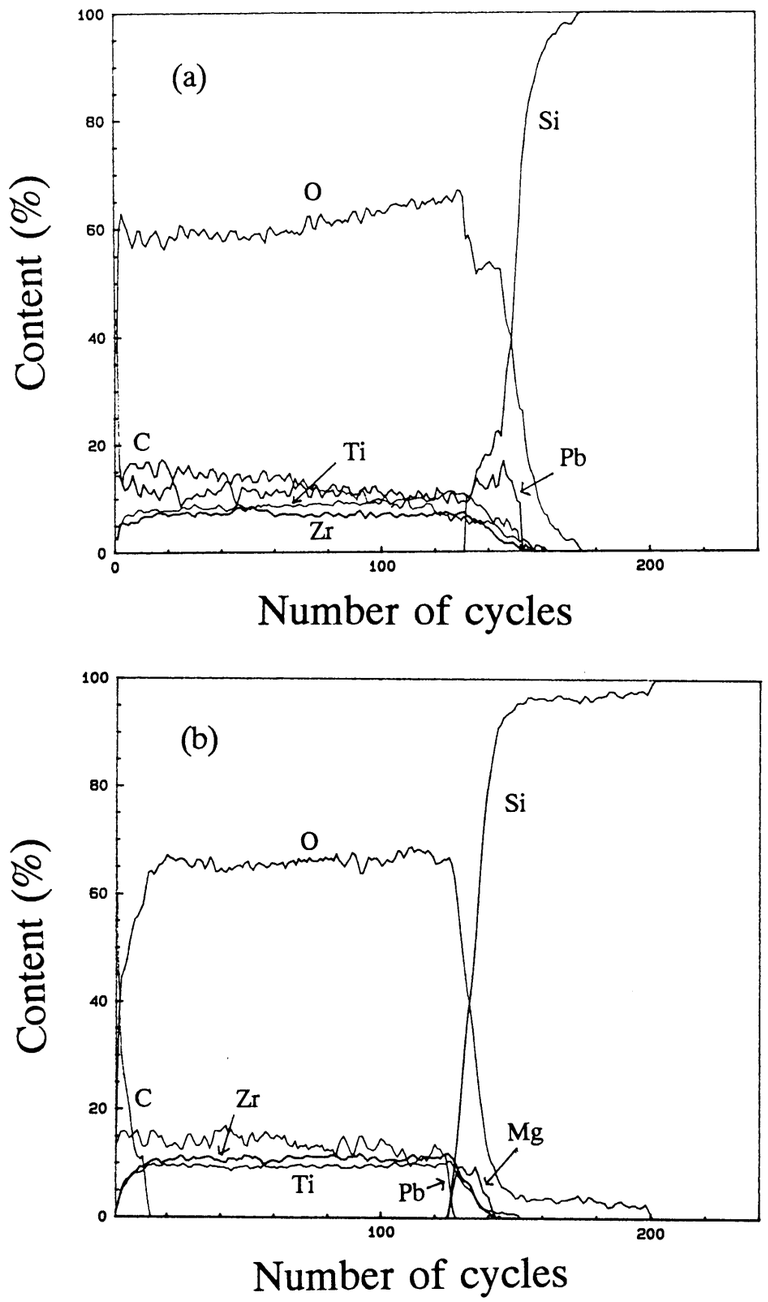

Fig. 3.14. AES depth profile of (a) PZT/Si structure without MgO buffer layer and (b) PZT/MgO/Si structure with MgO layer of 50 Å thickness.

μ m-thick MgO layer and a 0.3 μ m-thick PZT film are shown in Figs. 3.14 (a) and (b), respectively. It is shown in Fig. 3.15 (a) that the PZT surface is relatively smooth although some droplets are observed. Fig. 3.15 (b) suggests the columnar growth of both MgO layer and PZT films.

Polarization of a PZT/MgO/Si sample with MgO-layer thickness of 50 Å and with PZT-film thickness of 1 μ m was estimated using a Sawyer-Tower circuit at 60 Hz. The ferroelectric hysteresis loop is observed as shown in Fig. 3.16 although the shape in the hysteresis loop is not so excellent. The leakage-current density was quite large, as shown in Fig. 3.17, and it is possible that the large leakage current has an undesirable influence on the shape of the hysteresis loop. Improvement of these electrical properties is a problem to be solved.

3.6 *Summary*

MgO films were prepared on both (100)Si and (100)GaAs by EB evaporation under various deposition conditions. The orientation of MgO films on Si and GaAs changed from [111] to [100] with an increase in the substrate temperature or a decrease in the deposition rate. It also became apparent that MgO films become [100] oriented on (100)GaAs at lower temperature as compared with those on (100)Si. These results suggest the possibility of the orientation control of MgO films on semiconductor substrates by changing the deposition conditions. This orientation control of MgO films on semiconductor substrates will be a promising technology by which to fabricate monolithic devices composed of ferroelectric materials and semiconductors.

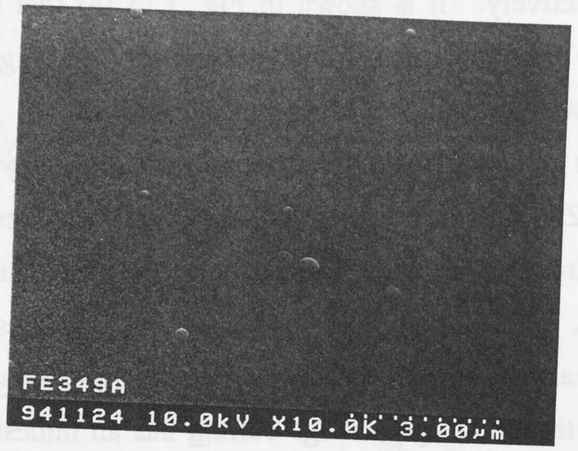

(a)

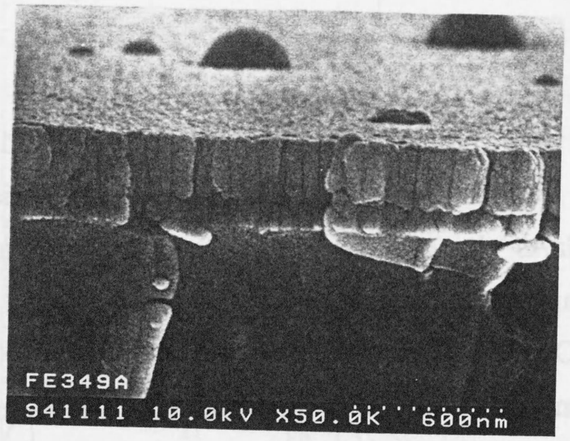

(b)

Fig. 3.15. FESEM images for (a) the surface and (b) the cross section of PZT/MgO/(100)Si structure.

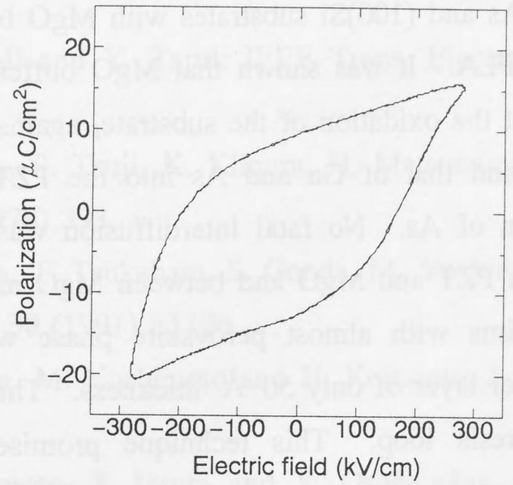

Fig. 3.16. Ferroelectric hysteresis loop estimated using a Sawyer–Tower circuit for PZT/MgO/Si structure with MgO–layer thickness of 50 Å and PZT–film thickness of 1 μ m.

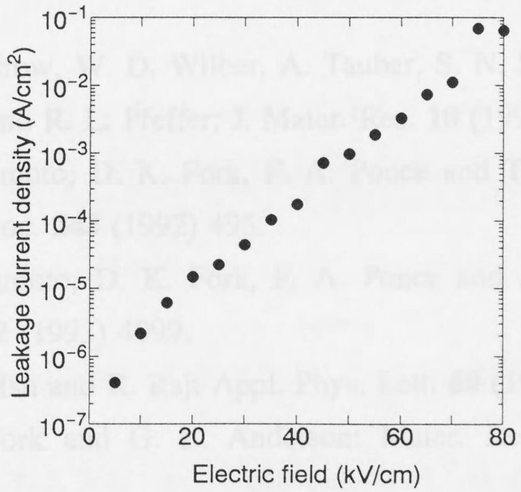

Fig. 3.17. Leakage–current density against the applied electric field for PZT/MgO/Si structure with MgO–layer thickness of 50 Å and PZT–film thickness of 1 μ m.

Highly [100]-oriented perovskite-phase PZT films were obtained by PLA on both (100)GaAs and (100)Si substrates with MgO buffer layer which was also prepared by PLA. It was shown that MgO buffer layer acts as an excellent barrier against the oxidation of the substrate, against the diffusion of Pb into the substrate and that of Ga and As into the PZT films, and also against the vaporization of As. No fatal interdiffusion was observed at the interfaces both between PZT and MgO and between MgO and GaAs or Si. [100]-oriented PZT films with almost perovskite phase were obtained on (100)Si with MgO buffer layer of only 50 Å thickness. This sample showed the ferroelectric hysteresis loop. This technique promises realization of integrated devices composed of semiconductors and ferroelectric materials, such as MFS-FETs.

References in Chapter 3

[1] J. L. Moll and Y. Tarui: IEEE Trans. Electron Devices **ED-10** (1963) 338.

[2] M. Ishida, S. Tsuji, K. Kimura, H. Matsunami and T. Tanaka: J. Cryst. Growth **45** (1978) 393.

[3] H. Nagata, T. Tsukahara, S. Gonda, M. Yoshimoto and H. Koinuma: Jpn. J. Appl. Phys. **30** (1991) L1136.

[4] H. Nagata, M. Yoshimoto and H. Koinuma: J. Cryst. Growth **118** (1992) 299.

[5] H. Fukumoto, T. Imura and Y. Osaka: Jpn. J. Appl. Phys. **27** (1988) L1404.

[6] D. K. Fork, F. A. Ponce, J. C. Tramontana and T. H. Geballe: Appl. Phys. Lett. **58** (1991) 2294.

[7] K. Nashimoto, D. K. Fork and T. H. Geballe: Appl. Phys. Lett. **60** (1992) 1199.

[8] S. C. Tidrow, W. D. Wilber, A. Tauber, S. N. Schauer, D. W. Eckart, R. D. Finnegan and R. L. Pfeffer: J. Mater. Res. **10** (1995) 1622.

[9] K. Nashimoto, D. K. Fork, F. A. Ponce and T. H. Geballe: Mater. Res. Soc. Symp. Proc. **243** (1992) 495.

[10] K. Nashimoto, D. K. Fork, F. A. Ponce and J. C. Tramontana: Jpn. J. Appl. Phys. **32** (1993) 4099.

[11] W. -Y. Hsu and R. Raj: Appl. Phys. Lett. **60** (1992) 3105.

[12] D. K. Fork and G. B. Anderson: Mater. Res. Soc. Symp. Proc. **285** (1993) 355.

[13] D. K. Fork and G. B. Anderson: Appl. Phys. Lett. **63** (1993) 1029.

[14] D. K. Fork, J. J. Kingston, G. B. Anderson, E. J. Tarsa and J. S. Speck:

Mater. Res. Soc. Symp. Proc. **310** (1993) 113.

[15] T. Hirai, K. Teramoto, T. Nishi, T. Goto and Y. Tarui: Jpn. J. Appl. Phys. **33** (1994) 5219.

[16] T. Hirai, K. Teramoto, K. Nagashima, H. Koike and Y. Tarui: Jpn. J. Appl. Phys. **34** (1995) 4163.

[17] E. Tokumitsu, K. Itani, B. -K. Moon and H. Ishiwara: Mater. Res. Soc. Symp. Proc. **361** (1995) 427.

[18] E. Tokumitsu, K. Itani, B. -K. Moon and H. Ishiwara: Jpn. J. Appl. Phys. **34** (1995) 5202.

[19] D. Dijkkamp, T. Venkatesan, X. D. Wu, S. A. Shaheen, N. Jisrawi, Y. H. Min-Lee, W. L. McLean and M. Croft: Appl. Phys. Lett. **51** (1987) 619.

[20] S. Otsubo, T. Minamikawa, Y. Yonezawa, T. Maeda, A. Moto, A. Morimoto and T. Shimizu: Jpn. J. Appl. Phys. **27** (1988) L2442.

[21] S. Otsubo, T. Maeda, T. Minamikawa, Y. Yonezawa, A. Morimoto and T. Shimizu: Jpn. J. Appl. Phys. **29** (1990) L133.

[22] H. Kidoh, T. Ogawa, A. Morimoto and T. Shimizu: Appl. Phys. Lett. **58** (1991) 2910.

[23] H. Kidoh, A. Morimoto and T. Shimizu: Appl. Phys. Lett. **59** (1991) 237.

[24] H. Kidoh, H. Yashima, A. Morimoto and T. Shimizu: Jpn. J. Appl. Phys. **33** (1994) 4094.

[25] A. Masuda, K. Matsuda, Y. Yonezawa, A. Morimoto and T. Shimizu: Jpn. J. Appl. Phys. Part 2. **35** (in press).

[26] E. J. Tarsa, M. De Graef, D. R. Clarke, A. C. Gossard and J. S. Speck: J. Appl. Phys. **73** (1993) 3276.

[27] A. J. SpringThorpe and P. Mandeville: J. Vac. Sci. & Technol. B**6** (1988) 754.

[28] D. K. Fork: private communication.

[29] *American Institute of Physics Handbook* (McGraw-Hill, New York) 2nd ed., p. 6-29.

[30] E. Fogarassy, F. Antoni, S. de Unamuno, C. Fuchs, J. Perriere and L. Ranno: AIP Conf. Proc. **288** (1994) 255.

[31] P. Tiwari, S. Sharan and J. Narayan: J. Appl. Phys. **69** (1991) 8358.

[32] Y. Yonezawa, K. Segawa, S. Katayama, T. Minamikawa, A. Morimoto and T. Shimizu: Jpn. J. Appl. Phys. **33** (1994) L1178.

[33] H. P. Klug and L. E. Alexander: *X-Ray Diffraction Procedures for Polycrystalline and Amorphous Materials* (Wiley, New York, 1974) Chap. 9.

Chapter 4 Plasma Nitridation of GaAs

4.1 *Background*

GaN is a direct wide band-gap semiconductor which has a stable phase with hexagonal wurtzite system, α -GaN, and has a metastable phase with cubic zinc-blende type, β -GaN. Both of crystal structures are shown in Fig. 4.1 [1]. GaN films and their alloy films with InN or AlN have attracted much attention for blue/green light emitting materials. These films are often prepared by metalorganic vapor phase epitaxy (MOVPE), molecular beam epitaxy (MBE) or hydride vapor phase epitaxy (HVPE), etc. on sapphire substrates. It was found that the GaN buffer layer deposited at low temperature plays an important role to obtain the high-quality hexagonal α -GaN films epitaxially grown on sapphire [2]. Metastable cubic β -GaN films can be grown on cubic substrates. For example, various attempts have been carried out to grow cubic β -GaN films on (100)GaAs by MOVPE [3-7] and MBE [8,9] after the first success by Mizuta *et al.* [10]. However hexagonal α -GaN films also grow on cubic substrates. For example, Yoshida *et al.* reported that hexagonal α - GaN films grow on the insufficiently nitrided (100)GaAs by gas-source MBE (GSMBE), while cubic β -GaN films grow on the (100)GaAs subjected to the sufficient nitridation using dimethylhydrazine (DMHy) [11,12]. Recently, Kikuchi *et al.* [13,14] also reported that the direct rf-radical nitridation of GaAs substrate before the GaN deposition control the crystal-structure of GaN films prepared by GSMBE. In this case, however, hexagonal α - GaN films are obtained on

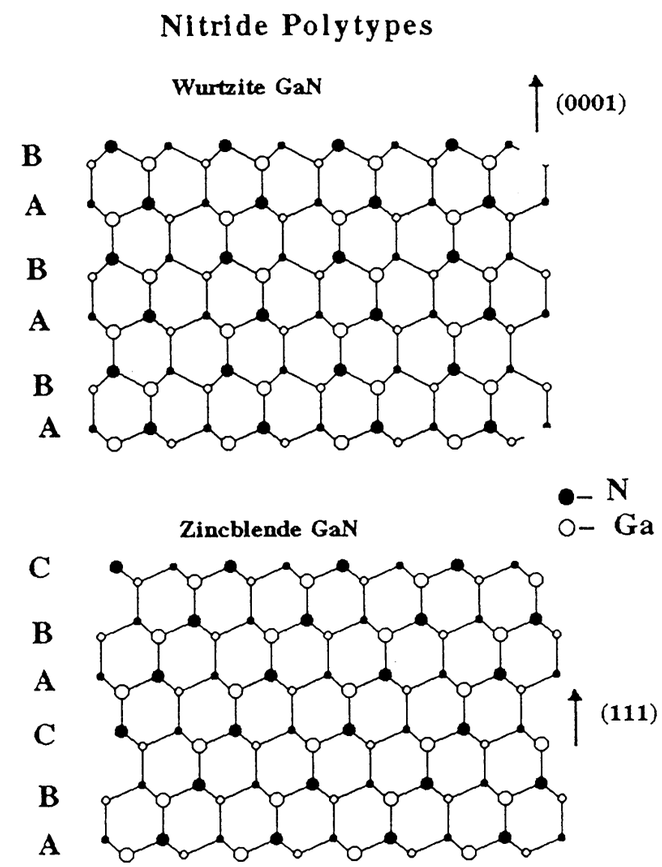

Fig. 4.1. Crystal structures of the GaN wurtzite and zinc-blende polytypes [1].

nitrided (100)GaAs and cubic β -GaN films are obtained on (100)GaAs without nitridation. Therefore the detail investigation on both the nitridation processes and the nitridation mechanism are inevitable for obtaining the appropriate nitrided layer as the buffer layer between cubic β -GaN films and GaAs substrate.

Recently, surface-nitridation mechanism of GaAs is studied using some spectroscopic methods. For example, X-ray photoelectron spectroscopy (XPS) [15], in situ photoluminescence (PL) [16] and in situ attenuated-total-reflection Fourier-transformation infrared (ATR-FTIR) spectroscopy [16,17] studies on the NH_3-plasma nitridation, reflection high-energy electron diffraction (RHEED) study on the N_2-plasma nitridation [18], X-ray diffraction (XRD) and Auger electron spectroscopy (AES) studies on the thermal and the plasma-assisted nitridation using NH_3 [19], XRD and RHEED studies on the thermal nitridation using NH_3 [20], scanning tunneling microscopy (STM) and atomic force microscopy (AFM) studies on the N radical nitridation [21], AES study on the electron-induced nitridation [22], XPS and high-resolution electron energy loss spectroscopy (HREELS) studies on the thermal nitridation using DMHy [23] and on the laser-assisted nitridation [24]. Especially, NTT Basic Research Laboratories group energetically studies on the thermal nitridation of (100)GaAs by N_2 through a hot W filament using RHEED [25-28], secondary ion mass spectrometry (SIMS) [25,26], IR reflectance spectroscopy [27], STM [28], transmission electron microscopy (TEM) [28] and PL [29]. However, the surface-nitridation mechanism has remained not so clear although high-quality GaN films on GaAs substrate, which are desirable due to the cleavability for fabricating the laser diode realized in the near future, are urgently required.

The nitridation of GaAs surface has also attracted much attention as important surface-passivation technique. Surface passivation is one of the most important processes for fabricating metal-insulator-semiconductor (MIS) structures in GaAs devices. In particular, the passivation for GaAs surface employing solutions such as $(NH_4)_2S$ or $(NH_4)_2S_x$ [30-33], $Na_2S \cdot 9H_2O$ [31,33,34], $P_2S_5/(NH_4)_2S$ [35,36] and NH_4I [37] has been the subject of intensive studies. It has been already confirmed that these processes are effective in reducing the surface-state density and the surface recombination velocity. However, such aqueous treatments cause contamination with heavy metals and have poor reproducibility. Alternative processes attracting much attention in recent years are dry passivations, which have some advantages over wet passivations. Firstly, better reproducibility is obtained in dry passivations than in wet ones because of more controllable process parameters. Secondly, a dry passivation can be a successive operation with other dry processes. For example, the insulator layer such as silicon nitride or silicon oxynitride can be deposited on the passivated GaAs surface successively and directly in the MIS fabrication process. A large number of methods for dry passivation of GaAs have been presented to date. For example, an rf H_2 plasma followed by an rf N_2 plasma [38,39], an electron cyclotron resonance (ECR) N_2+H_2 plasma [40], an rf [15,41] and a microwave [15] NH_3 plasma, an N_2^+ ion beam [42] and a simultaneous irradiation with a molecular NH_3 flux and a pulsed excimer laser [24] or an electron beam [22] are used for the nitridation. An rf H_2S plasma [43] and an ArF excimer laser irradiation in an H_2S ambient [44] are used for sulfidation. An rf PH_3+H_2 plasma [45] is used for phosphidization. In dry passivations, improved surface qualities and/or device performances have been also confirmed [39-41,43,45]. Therefore investigation on the detailed mechanism for the nitridation of GaAs is also

urgently required from the viewpoint of developing the better dry-passivation process.

In this study the GaAs surface reaction with NH_3 plasma is reported and the plasma-nitridation mechanism is discussed. XPS study with varying the photoelectron take-off angle is carried out to study the detailed process and mechanism in the surface reaction. It is found that appropriate nitridation condition brings about the GaN layer on GaAs although unstable Ga-As-N or As-N layer is also formed under unsuitable conditions. The improvement of such unstable layers is achieved by the excimer-laser irradiation. The oxidation resistance in the plasma-nitrided GaAs surface is also investigated.

4.2 *Nitridation for various times and at various temperatures*

In this section NH_3-plasma nitridation process of (100)GaAs is discussed based on the results obtained by XPS. Changes with the NH_3-plasma-treatment time in both Ga 3*d* and As 3*d* XPS spectra are shown in Fig. 4.2 for samples treated at 250 ℃, and those with the plasma-treatment temperature are shown in Fig. 4.3 for samples treated for 20 min. All spectra were observed at the photoelectron take-off angle θ of 90°. The closed circles indicate the signals due to GaAs substrate. XPS spectra for GaAs substrate before the plasma treatment, just after the aqueous treatment mentioned in § 2.1.3, are also shown in Fig. 4.2. It is found that the aqueous treatment almost completely etches the surface oxide, which is known to give an XPS signal with higher binding energy (BE) than GaAs substrate both in Ga 3*d* and in As 3*d* spectra. The remarkable change with the plasma treatment observed in Fig. 4.2 is the appearance of new signals with higher

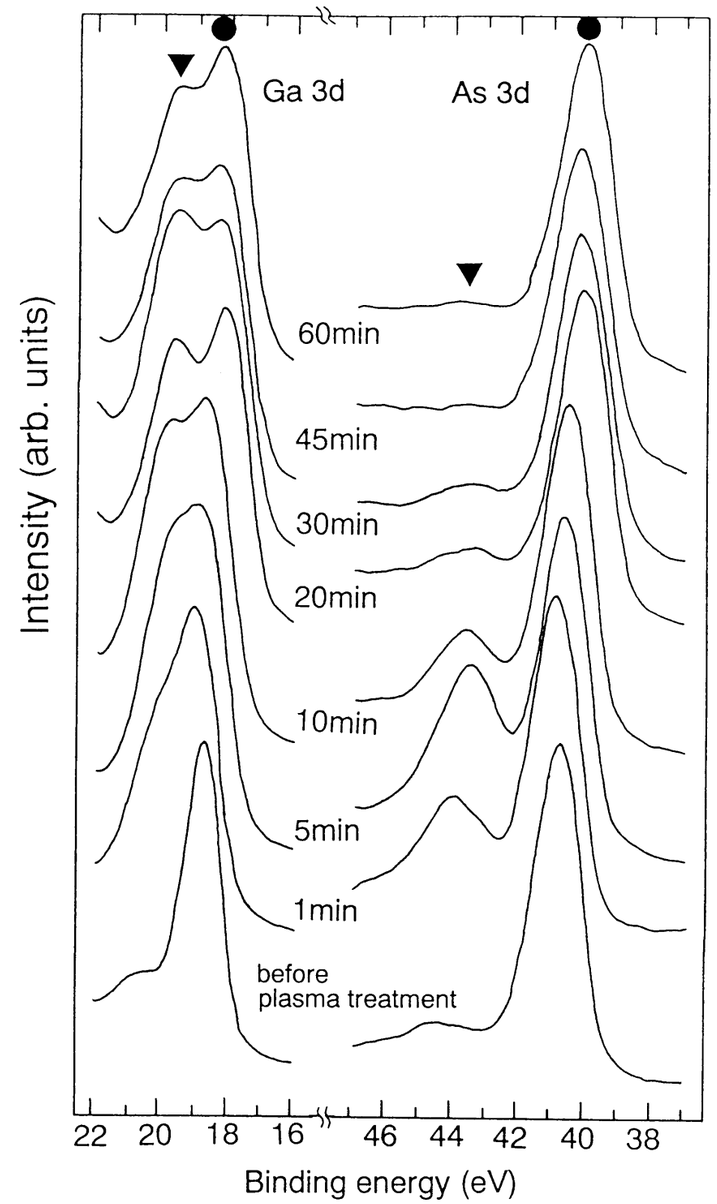

Fig. 4.2. Changes in Ga 3*d* and As 3*d* XPS spectra for samples subjected to NH_3-plasma treatment at 250 ℃ for various times. Spectra for GaAs before plasma treatment, just after aqueous treatment, are also shown. Closed circles and triangles represent the signals due to GaAs and those due to nitride, respectively.

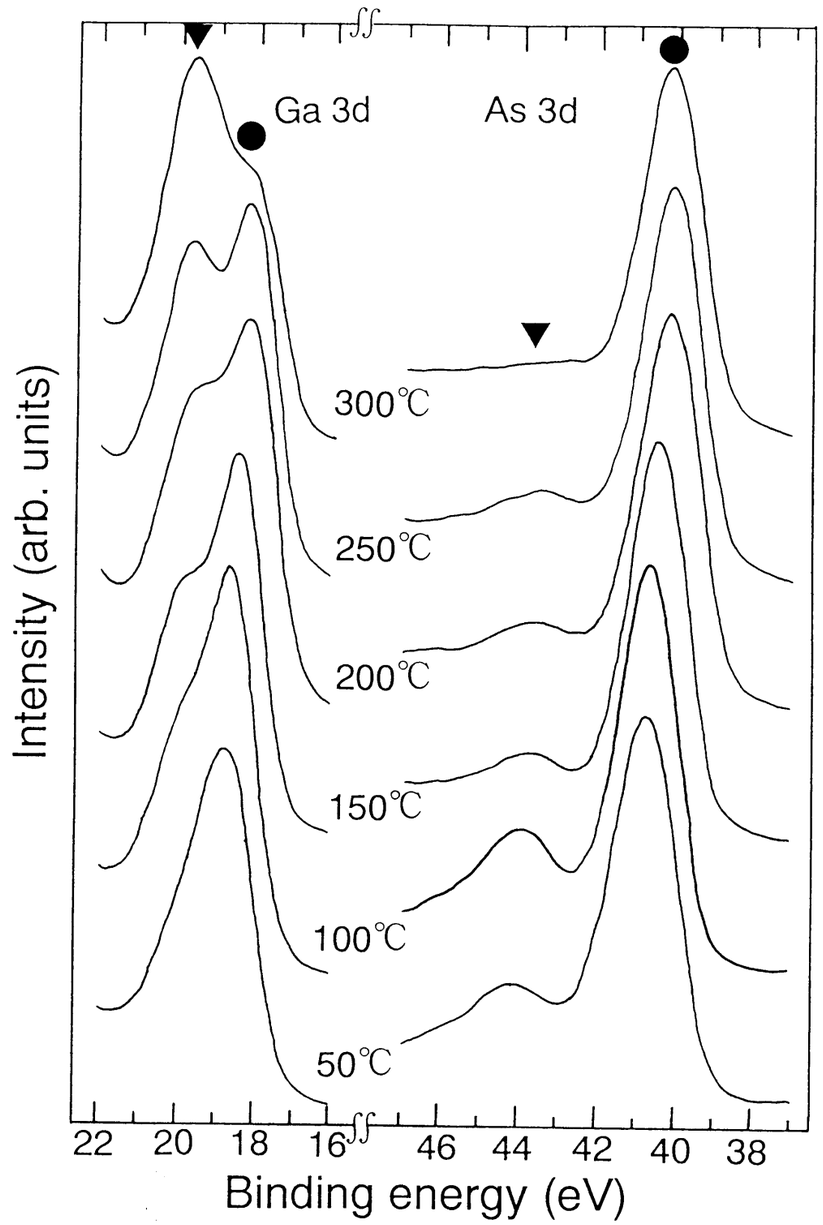

Fig. 4.3. Changes in Ga 3*d* and As 3*d* XPS spectra for samples subjected to NH_3–plasma treatment for 20 min at various temperatures. Closed circles and triangles represent the signals due to GaAs and those due to nitride, respectively.

BE shown by closed triangles both in Ga 3*d* and in As 3*d* spectra. The new signal in As 3*d*, however, decreases and then disappears with increasing treatment time, although it initially increases. A similar change with increasing plasma–treatment temperature is observed in Fig. 4.3. The fact that the signals due to GaAs are observed in all the spectra means that the layer causing the new XPS signal with high BE, formed by the plasma treatment, has a thickness of only several tens of Å, from considerations of the photoelectron escape depth.

The differences in BE observed in Ga 3*d* spectra between the new signal shown by a closed triangle and the original signal due to GaAs substrate shown by a closed circle for samples treated at 250 ℃ and for those treated for 20 min are shown in Figs. 4.4 and 4.5, respectively. The BE difference in Ga 3*d* gradually increases as the treatment time or treatment temperature increases and saturates after the treatment for 20 min or for the treatment at over 250 ℃. This new signal observed in Ga 3*d* is assumed to result from the nitride layer formed by the plasma treatment. The increase in the BE difference in Ga 3*d* is ascribed to the desorption of As from the nitride layer. In the As 3*d* spectra shown in Figs. 4.2 and 4.3, the disappearance of the signal shown by a closed triangle with plasma treatment exceeding 20 min or that above 200 ℃ is noteworthy. The BE difference in As 3*d* spectra between the signal due to GaAs and that shown by a closed triangle is smaller than that between the signal due to GaAs and the oxides. The XPS intensity of the N 1*s* signal is also shown in Fig. 4.4 as a function of the plasma–treatment time and in Fig. 4.5 as a function of the plasma–treatment temperature. Here the intensity of the sample treated for 1 min in Fig. 4.4 or treated at 50 ℃ in Fig. 4.5 is normalized to 1. The behavior of the XPS intensity of the N 1*s* signal shown in Fig. 4.4 is similar to that of the signal

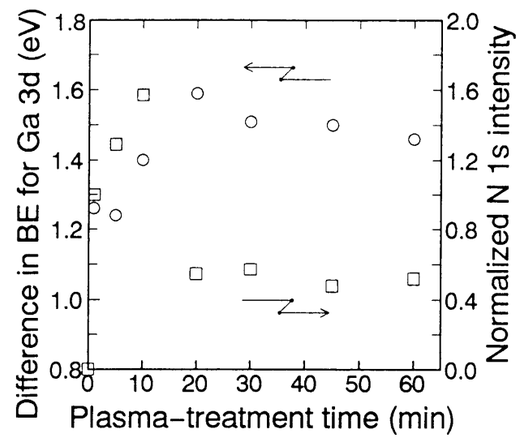

Fig. 4.4. Open circles show BE difference for Ga 3*d* XPS spectra between the signal shown by the closed circles and that by the closed triangles in Fig. 4.2 as a function of NH_3-plasma-treatment time. Normalized N 1*s* intensity against NH_3-plasma-treatment time is also shown with open squares. Samples were treated at 250 ℃.

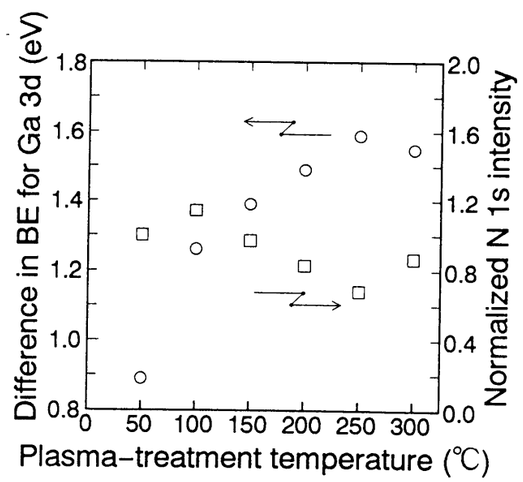

Fig. 4.5. Open circles show BE difference for Ga 3*d* XPS spectra between the signal shown by the closed circles and that by the closed triangles in Fig. 4.3 as a function of NH_3-plasma-treatment temperature. Normalized N 1*s* intensity against NH_3-plasma-treatment temperature is also shown with open squares. Samples were treated for 20 min.

shown by a closed triangle in As 3*d* spectra in Fig. 4.2. A similar relationship is also found between Figs. 4.3 and 4.5. These facts suggest that the signals with higher BE in As 3*d* spectra, shown by the closed triangles in Figs. 4.2 and 4.3, is not due to As-O bonds in the suboxide but due to As-N bonds. The existence of such As-N bonds were recently confirmed also by other groups in the nitridation of GaAs using atomic N generated with a heated W filament [27] and using ECR NH_3 plasma [46] after this study. The enhancement of the BE difference in Ga 3*d* spectra and the reduction of the signal due to As-N bonds, both of which tend to saturate after the treatment of 20 min, as shown in Fig. 4.4, clarify the surface reaction of GaAs with NH_3 plasma. Namely, the Ga-As-N layer is formed on GaAs in the early stage, and then the GaN layer is mainly formed by desorption of As and N bonded to As from such ternary compounds. The desorption of N bonded to As is suggested by the decrease in N 1*s* intensity of the sample treated for 10 min to that of the sample treated for 20 min, shown in Fig. 4.4, corresponding to the decrease in the signal due to As-N bonds, shown in Fig. 4.2. In the case of samples treated for 20 min at various temperatures, the GaN layer is also formed on GaAs in the same manner when treatment temperature exceeds 200 ℃.

We refer to N 1*s* XPS spectra in detail. N 1*s* XPS spectra show a single-peak signal whose peak position is about 398.5 eV, but also have a small shoulder whose peak position is about 401 eV in the case of treatments for 20 min above 150 ℃. The samples treated at 250 ℃ show such a shoulder in N 1*s* spectra regardless of the treatment time. The ratio of the shoulder with high BE to the total N 1*s* signal intensity is around 10 – 20 % with a few exceptions. The origin of the shoulder is still unknown. The "XPS intensity of N 1*s*" in the foregoing and the following paragraph means

the intensity of the main signal estimated by the signal separation.

The detailed surface reaction between GaAs surface and NH_3 plasma is analyzed by angle-dependent XPS (ADXPS) described in § 2.2.1. Figure 4.6 shows the normalized XPS intensities mentioned in § 2.2.1 of Ga 3*d* and As 3*d* both due to nitride and N 1*s* as a function of the photoelectron take-off angle θ for samples treated at 250 ℃ for 1, 5, 10 and 20 min. Taking the principles of ADXPS mentioned in § 2.2.1 into account, namely, considering that smaller θ gives information in the region nearer to the surface, it is found that the intensity of As due to nitride decreases in the surface region as the treatment time increases. Therefore the surface nitridation mechanism with increasing treatment time is suggested to be as follows. In the early stage of the treatment Ga-As-N ternary compounds, which contain As-N bonds and are not $GaAs_xN_{1-x}$ mixed crystal, are formed on GaAs substrate. As the NH_3-plasma treatment proceeds, a GaN layer is gradually formed on the GaAs substrate by the desorption of both As and N bonded to As from Ga-As-N ternary compounds. The surface layer formed by the treatment for longer than 20 min is mainly GaN without As.

The normalized XPS intensities for samples treated for 20 min at various temperatures are shown in Fig. 4.7 in the same manner as in Fig. 4.6. Both the intensities of As 3*d* due to nitride and N 1*s* increase as θ decreases for the sample treated at 50 ℃. All the intensities of Ga 3*d* and As 3*d* both due to nitride and N 1*s* are increased with decreasing θ for the sample treated at 100 ℃. It also turns out for the samples treated above 200 ℃ that as θ decreases, both the intensities of Ga 3*d* due to nitride and N 1*s* increase, but the intensity of As 3*d* due to nitride is constant regardless of θ. These results suggest that the composition of the surface layer varies with the treatment temperature: As-N binary compounds at 50 ℃, Ga-As-N ternary

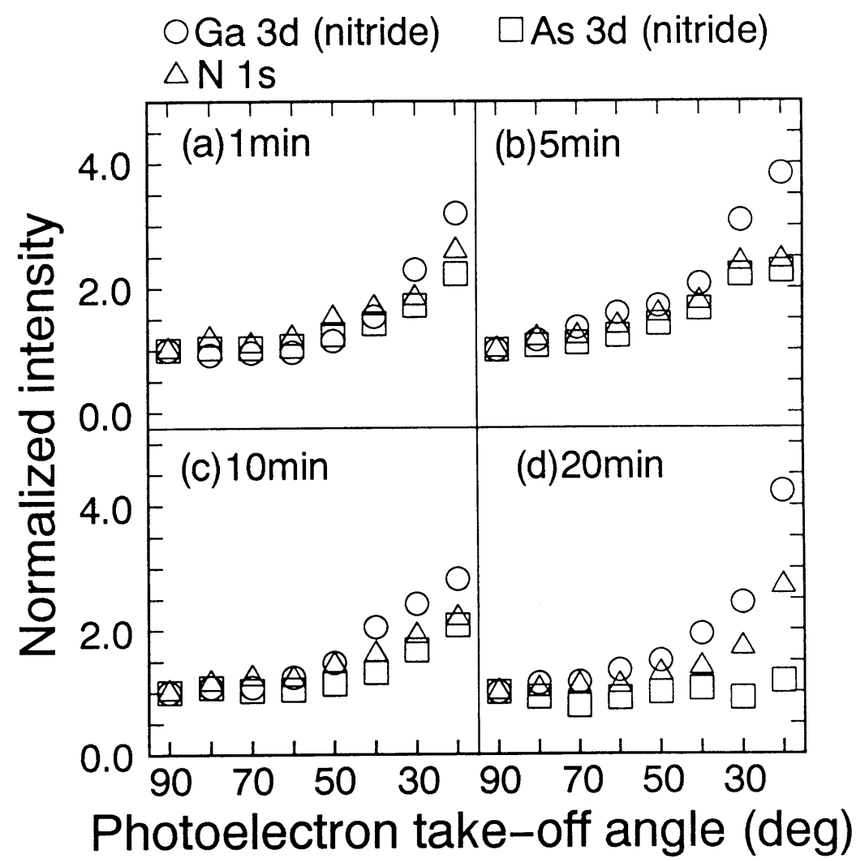

Fig. 4.6. Normalized XPS intensities of Ga 3*d* due to nitride, As 3*d* due to nitride and N 1*s* against the photoelectron take-off angle. Plasma-treatment temperature is 250 ℃ and plasma-treatment times are (a) 1 min, (b) 5 min, (c) 10 min and (d) 20 min.

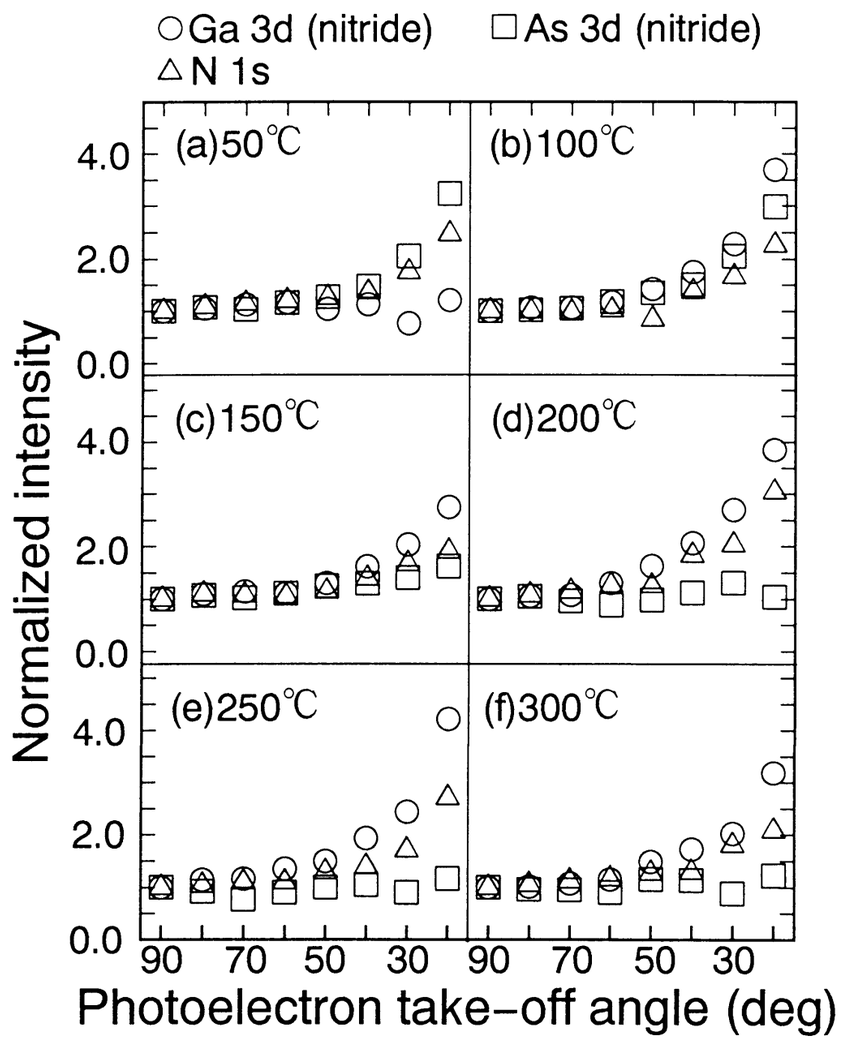

Fig. 4.7. Normalized XPS intensities of Ga 3*d* due to nitride, As 3*d* due to nitride and N 1*s* against the photoelectron take-off angle. Plasma-treatment time is 20 min and plasma-treatment temperatures are (a) 50 ℃, (b) 100 ℃, (c) 150 ℃, (d) 200 ℃, (e) 250 ℃ and (f) 300 ℃.

compounds at 100 ℃ and mainly GaN at higher than 200 ℃.

It is clarified from Figs. 4.6 and 4.7 that increasing treatment time and temperature play similar roles for forming the GaN layer. The surface-nitridation mechanism is schematically illustrated and summarized in Fig. 4.8. The compositions of GaN layer formed by the plasma treatment at 250 ℃ for longer than 20 min and by that for 20 min at higher than 200 ℃ were confirmed by XPS to be almost stoichiometric.

4.3 *Nitridation mechanism*

Nitridation mechanism of GaAs will be discussed in this section based on some experimental results. The XPS intensity of Ga 3*d* signal due to nitride is shown in Fig. 4.9 as a function of the plasma-nitridation temperature for samples nitrided for 20 min. The solid line in Fig. 4.9 was obtained using least squares. It is clear that the intensity follows the Arrhenius plot. The activation energy estimated is 35 meV. This low activation energy suggests that the contribution of the thermal reaction and/or the thermal diffusion of nitrogen species is not dominant for the plasma-nitridation.

The ratio of the intensity of the Ga 3*d* signal due to nitride to the total intensity of Ga 3*d*, designated as GaN fraction, is shown in Fig. 4.10 as a function of the plasma-nitridation time for samples nitrided at 250 ℃. It was found that the nitridation rapidly proceeds within 1 min, and then proceeds linearly with the nitridation time for the nitridation longer than 1 min. The rapid nitridation in the early stage is supposed to originate from the direct reaction of species in NH_3 plasma with the GaAs surface. It is also expected that the smaller nitridation rate than that in the early stage originates

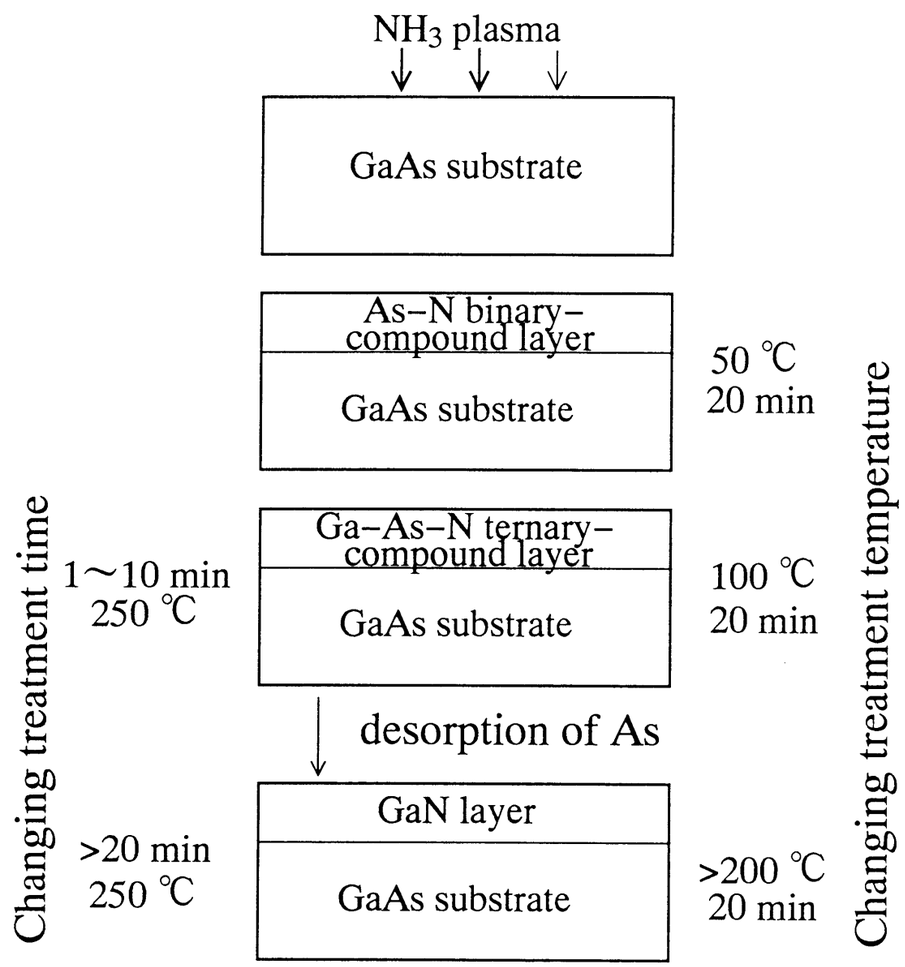

Fig. 4.8. Schematic diagram of the model for surface reaction of GaAs with NH_3 plasma.

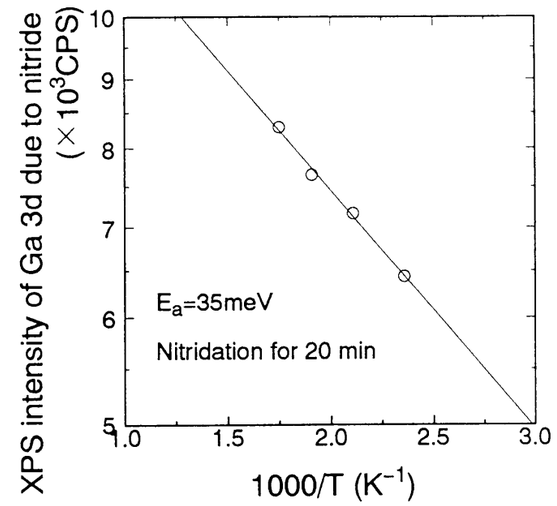

Fig. 4.9. XPS intensity of Ga 3*d* due to nitride against the nitridation temperature for samples nitrided for 20 min. Solid lines were obtained using least squares.

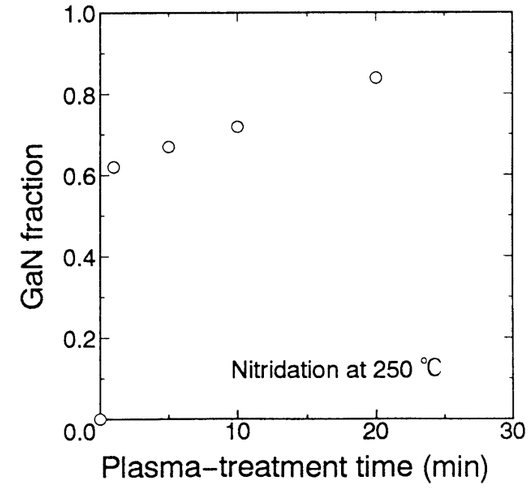

Fig. 4.10. GaN fraction defined in the text against the nitridation time for samples nitrided at 250 ℃.

from the event that the reaction of species in NH_3 plasma with GaAs occurs at the interface between the nitrided layer and GaAs, and those species are required to pass through the nitrided layer.

The substrate-orientation dependence of the plasma nitridation was also studied. It was confirmed as shown in Figs. 4.11 that both (111)A and (111)B GaAs surfaces nitrided at 250 ℃ for 1 min consist of Ga-As-N ternary compounds in the same manner as (100)GaAs shown in Fig. 4.6 (a). Also in the case of the nitridation for 5 min, similar results were obtained. The normalized N 1*s* intensities for (111)A, (111)B and (100)GaAs nitrided for 5 min are shown in Fig. 4.12. There was no remarkable difference in the N 1*s* signal intensity between (111)A and (111)B GaAs although the N 1*s* signal intensity for (111)GaAs was 2 or 3 times larger than that for (100)GaAs. The normalized XPS intensity for As 3*d* signal due to nitride against θ is shown in Fig. 4.13 for (111)A and (111)B GaAs nitrided for 5 min at 250 ℃. Although no large difference was observed in the number of Ga-N bonds between (111)A and (111)B surfaces, it is found from Fig. 4.13 that a larger number of As-N bonds exist for (111)B surface than for (111)A surface. This fact is supposed to originate from the As-stabilized surface of (111)B GaAs, and suggests the possibility of the layer-by-layer nitridation.

4.4 *Oxidation resistance of the nitrided layer*

Next, the oxidation resistance of (100)GaAs after this plasma treatment will be reported. Figure 4.14 shows As 3*d* XPS spectra at θ of 90° for the sample subjected to the plasma treatment at 250 ℃ for 45 min after the aqueous treatment mentioned in § 2.1.3 and one subjected only to the

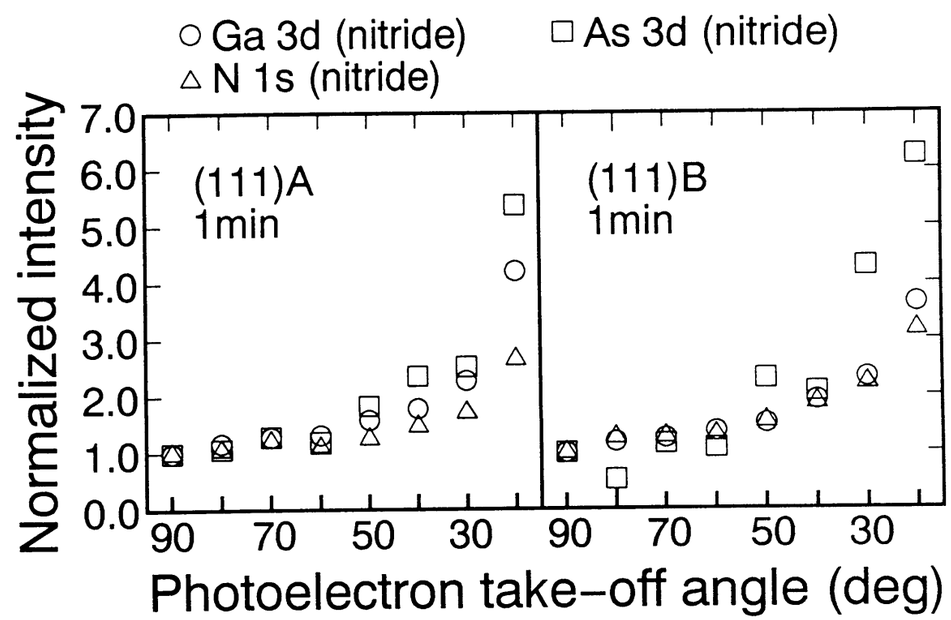

Fig. 4.11. Normalized XPS intensities of Ga 3*d* due to nitride, As 3*d* due to nitride and N 1*s* against the photoelectron take-off angle for (111)A and (111)B GaAs nitrided at 250 ℃ for 1 min.

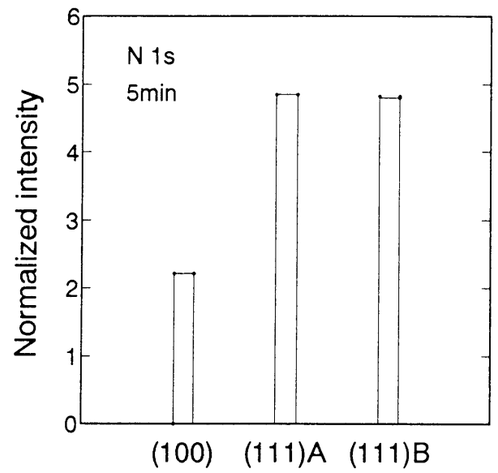

Fig. 4.12. Normalized XPS intensity of N 1*s* for (111)A, (111)B and (100)GaAs nitrided at 250 ℃ for 5 min.

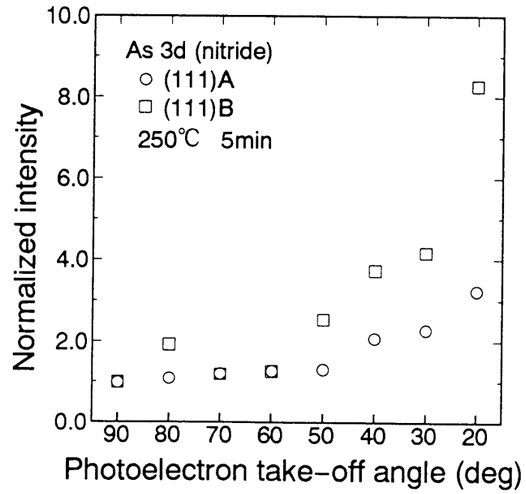

Fig. 4.13. Normalized XPS intensity of As 3*d* due to nitride against the photoelectron tale-off angle for (111)A and (111)B GaAs nitrided at 250 ℃ for 5 min.

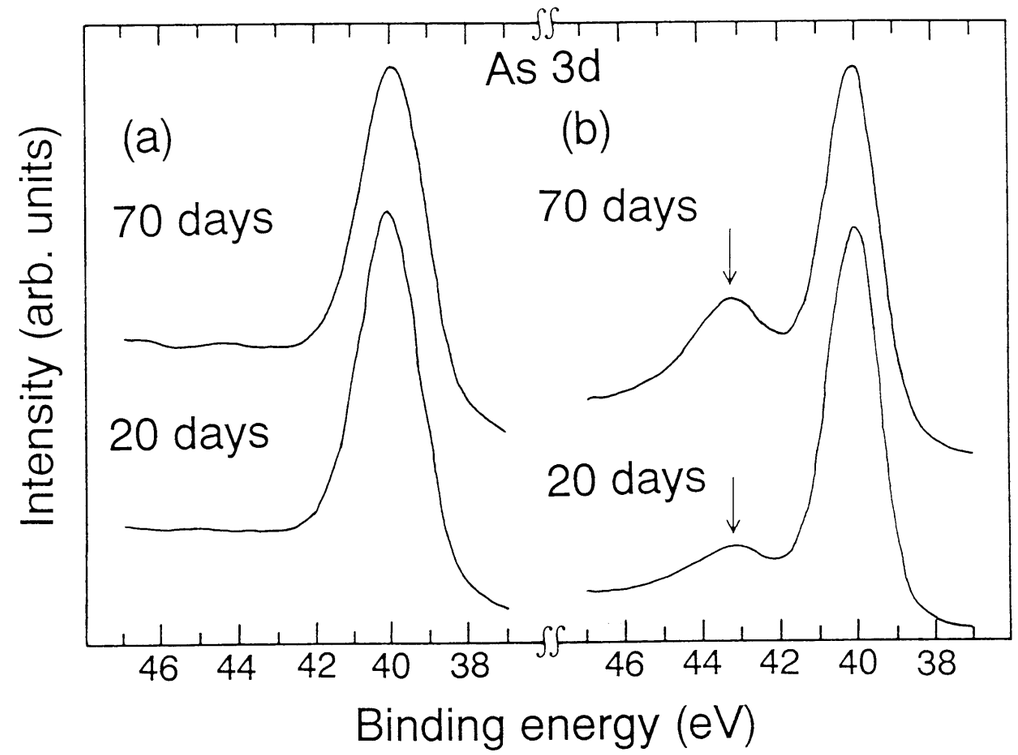

Fig. 4.14. As 3*d* XPS spectra for samples (a) subjected to the plasma treatment at 250 ℃ for 45 min and (b) only subjected to the aqueous treatment. XPS spectra were observed after air exposure for 20 days and 70 days.

aqueous treatment. The surface of the plasma-treated sample is covered with the GaN layer as mentioned in § 4.2. The XPS observations were carried out after the air exposure at room temperature (RT) for 20 days and 70 days. There are almost no signals due to oxide in As 3*d* XPS spectra after the aforementioned plasma or aqueous treatments as shown in Fig. 4.2. This means that both the treatments are effective methods for etching the native oxide on GaAs surface. However, the air exposure results in the signal due to oxide, shown by the arrows in Fig. 4.14, in the sample subjected only to the aqueous treatment. On the other hand, almost no signal due to oxide can be observed in the plasma-treated sample even after the air exposure for 70 days. These results guarantee the validity of the NH_3-plasma treatment for the passivation of GaAs surface for many hours.

4.5 *Excimer-laser irradiation on the nitrided layer*

Excimer-laser irradiation was attempted for improving the unstable nitrided layer containing As-N bonds on (100)GaAs formed by low-temperature or short-time nitridation. Irradiation was carried out for 1 min in a vacuum and detailed irradiation conditions were shown in § 2.1.3. Figure 4.15 shows the normalized XPS signal intensity, defined in § 2.2.1, for As 3*d* signal due to nitride against the photoelectron take-off angle θ before and after the laser irradiation at RT. Before the laser irradiation, the plasma nitridation was carried out at (a) 50 ℃ for 20 min, (b) 100 ℃ for 20 min and (c) 250 ℃ for 5 min. The surface layer before the irradiation was As-N binary compounds for (a) and Ga-As-N ternary compounds for (b) and (c). The number of Ga-N bonds was far smaller than that of As-N bonds for

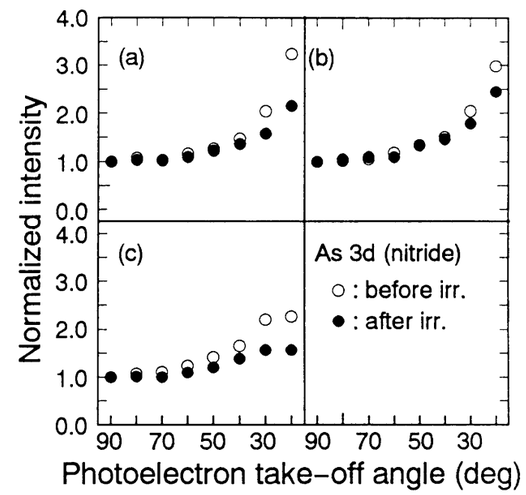

Fig. 4.15. Normalized XPS intensity of As 3*d* due to nitride against the photoelectron take-off angle before and after the laser irradiation at RT. Before laser irradiation, plasma nitridation was carried out at (a) 50 ℃ for 20 min, (b) 100 ℃ for 20 min and (c) 250 ℃ for 5 min.

(a) and larger than that of As–N bonds for (b) and (c). It is revealed from Fig. 4.15 that the laser irradiation at RT decreases the number of As–N bonds in the surface layer. The laser irradiation was also performed at elevated temperatures. As 3*d* XPS spectra at θ of 20 deg for samples nitrided at 50 ℃ for 20 min before the laser irradiation, after the laser irradiation at RT, 80 ℃ and 150 ℃ are shown in Fig. 4.16. The circular and the triangular symbols show the signal due to GaAs substrate and As–N bonds, respectively. The signal due to As–N bonds decreases with the laser irradiation at RT as also shown in Fig. 4.15. Most of As–N bonds disappear with the laser irradiation above 80 ℃ for only 1 min. Figure 4.17 shows the normalized XPS intensities of Ga 3*d* due to nitride, As 3*d* due to nitride and N 1*s* against photoelectron tale–off angle for GaAs annealed at 150 ℃ for 10 min in the vacuum of the order of 10^{-5} Pa following the nitridation at 50 ℃ for 20 min. Little difference is observed between the normalized ADXPS intensity of As 3*d* due to nitride shown in Fig. 4.17 and that observed for GaAs only with the nitridation at 50 ℃ for 20 min shown in Fig. 4.7 (a). Therefore it is confirmed that elevated temperature without laser irradiation brings about little decrease in the number of As–N bonds. The possible reason for the disappearance of unstable As–N bonds with the laser irradiation is the bond breaking with the temperature increase and/or with the electronic excitation. Figure 4.18 shows the normalized XPS intensity for Ga 3*d* signal due to nitride against θ before and after the laser irradiation. Although few Ga–N bonds were observed before the irradiation, GaN became the dominant element in the surface layer after the irradiation.

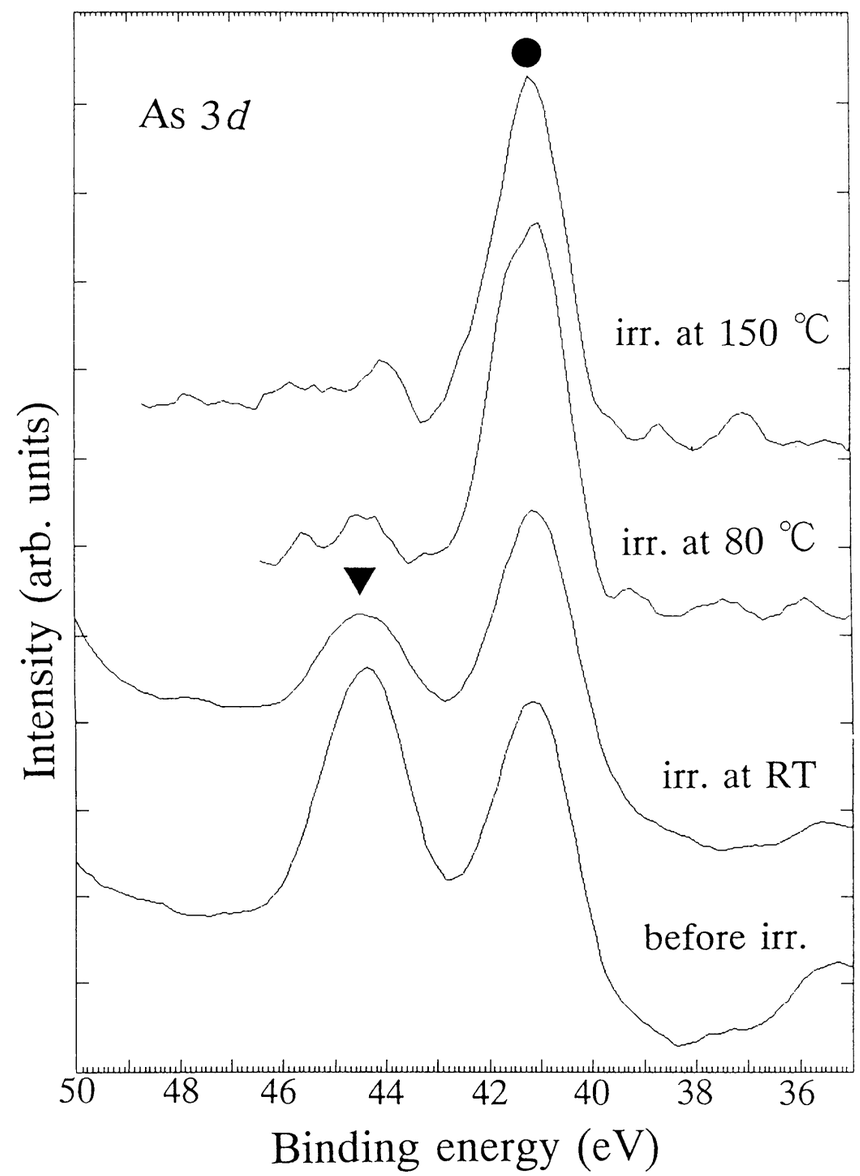

Fig. 4.16. As 3*d* XPS spectra before and after the laser irradiation at various temperatures. Circular and triangular symbols show the signal due to GaAs substrate and As–N bonds, respectively.

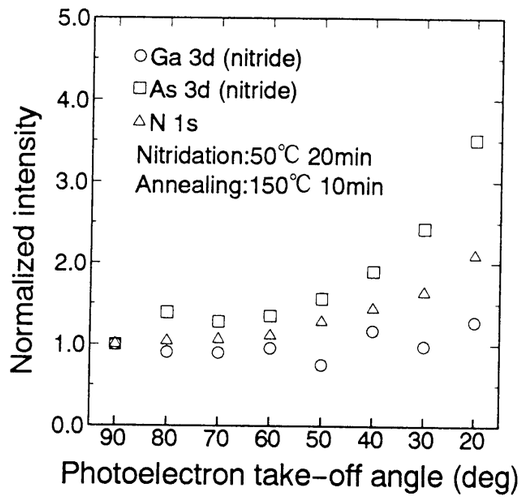

Fig. 4.17. Normalized XPS intensities of Ga 3*d* due to nitride, As 3*d* due to nitride and N 1*s* against the photoelectron take-off angle for (100)GaAs annealed at 150 ℃ for 10 min following the nitridation at 50 ℃ for 20 min.

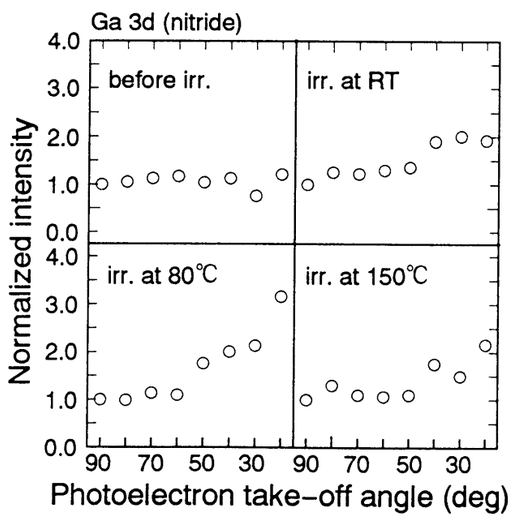

Fig. 4.18. Normalized XPS intensity of Ga 3*d* due to nitride against the photoelectron take-off angle before and after the laser irradiation at various temperatures.

4.6 *Summary*

NH_3-plasma nitridation of (100)GaAs with a planar magnetic field were carried out at various temperatures and for various times. The surface reaction of GaAs with NH_3 plasma was studied in detail using ADXPS. It is revealed that the surface composition varies with the plasma-nitridation time and temperature. First, an unstable As-N or Ga-As-N layer is formed on the GaAs surface. Then, such unstable layer disappears with increasing treatment time or temperature. The formation of a GaN layer on GaAs surface can be achieved with the appropriate treatment time and temperature. NH_3-plasma nitridation mainly proceeds without the thermal reaction and/or the thermal diffusion. The nitridation proceeds faster for (111)GaAs than for (100)GaAs. Although the nitridation rate for (111)B is equal to that for (111)A, a larger number of As-N bonds are observed in (111)B surface than in (111)A surface. Successive laser irradiation after the plasma nitridation decreases the number of As-N bonds in the unstable surface layer and enhances the GaN formation. This process is confirmed to be also one of the promising candidates for the surface passivation of GaAs.

References in Chapter 4

[1] H. Morkoc, S. Strite, G. B. Gao, M. E. Lin, B. Sverdlov and M. Burns: J. Appl. Phys. **76** (1994) 1363.

[2] S. Nakamura: Jpn. J. Appl. Phys. **30** (1991) L1705.

[3] Y. Nitta, K. Onabe, S. Fukatsu, Y. Shiraki and R. Ito: *Proc. 10th Symp. Alloy Semiconductor Physics and Electronics, Nagoya, 1991*, p. 173.

[4] S. Fujieda and Y. Matsumoto: Jpn. J. Appl. Phys. **30** (1991) L1665.

[5] S. Miyoshi, K. Onabe, N. Ohkouchi, H. Yaguchi, R. Ito, S. Fukatsu and Y. Shiraki: J. Cryst. Growth **124** (1992) 439.

[6] N. Kuwano, Y. Nagatomo, K. Kobayashi, K. Oki, S. Miyoshi, H. Yaguchi, K. Onabe and Y. Shiraki: Jpn. J. Appl. Phys. **33** (1994) 18.

[7] M. Sato: J. Appl. Phys. **78** (1995) 2123.

[8] H. Okumura, S. Misawa and S. Yoshida: Appl. Phys. Lett. **59** (1991) 1058.

[9] S. Strite, J. Ruan, Z. Li, A. Salvador, H. Chen, D. J. Smith, W. J. Choyke and H. Morkoc: J. Vac. Sci. & Technol. B**9** (1991) 1924.

[10] M. Mizuta, S. Fujieda, Y. Matsumoto and T. Kawamura: Jpn. J. Appl. Phys. **25** (1986) L945.

[11] S. Yoshida, H. Okumura, S. Misawa and E. Sakuma: Surf. Sci. **267** (1992) 50.

[12] H. Okumura, S. Yoshida, S. Misawa and E. Sakuma: J. Cryst. Growth **120** (1992) 114.

[13] A. Kikuchi, H. Hoshi, K. Kishino: *Extended Abstracts 1993 Int. Conf. Solid State Devices and Materials, 1993, Chiba*, p. 110.

[14] A. Kikuchi, H. Hoshi and K. Kishino: Jpn. J. Appl. Phys. **33** (1994) 688.

[15] E. S. Aydil, K. P. Giapis, R. A. Gottscho, V. M. Donnelly and E. Yoon: J. Vac. Sci. & Technol. B**11** (1993) 195.

[16] E. S. Aydil, Z. Zhou, K. P. Giapis, Y. Chabal, J. A. Gregus and R. A. Gottscho: Appl. Phys. Lett. **62** (1993) 3156.

[17] E. S. Aydil, Z. H. Zhou, R. A. Gottscho and Y. J. Chabal: J. Vac. Sci. & Technol. B**13** (1995) 258.

[18] R. J. Hauenstein, D. A. Collins, X. P. Cai, M. L. O'Steen and T. C. McGill: Appl. Phys. Lett. **66** (1995) 2861.

[19] M. E. Jones, J. R. Shealy and J. R. Engstrom: Appl. Phys. Lett. **67** (1995) 542.

[20] A. Yamamoto, Y. Yamauchi, M. Ohkubo, A. Hashimoto and T. Saitoh: *Proc. Topical Workshop on III - V Nitrides, Nagoya, 1995*, to be published.

[21] H. Sugiyama, M. Shinohara and K. Wada: *Proc. Topical Workshop on III - V Nitrides, Nagoya, 1995*, to be published.

[22] Y. -M. Sun and J. G. Ekerdt: J. Vac. Sci. & Technol. B**11** (1993) 610.

[23] Y. -M. Sun, D. W. Sloan, M. McEllistrem, A. L. Schwaner and J. M. White: J. Vac. Sci. & Technol. A**13** (1995) 1455.

[24] X. -Y. Zhu, M. Wolf and J. M. White: J. Vac. Sci. & Technol. A**11** (1993) 838.

[25] T. Makimoto and N. Kobayashi: Appl. Phys. Lett. **67** (1995) 548.

[26] T. Makimoto and N. Kobayashi: Appl. Surf. Sci., to be published.

[27] K. Uwai, Y. Yamauchi and N. Kobayashi: Appl. Surf. Sci., to be published.

[28] M. Kasu, T. Makimoto and N. Kobayashi: submitted to Appl. Phys. Lett.

[29] T. Makimoto and N. Kobayashi: Appl. Phys. Lett. **67** (1995) 688.

[30] J. -F. Fan, H. Oigawa and Y. Nannichi: Jpn. J. Appl. Phys. **27** (1988) L1331.

[31] M. S. Carpenter, M. R. Melloch, M. S. Lundstrom and S. P. Tobin: Appl.

Phys. Lett. **52** (1988) 2157.

[32] Y. Nannichi, J. -F. Fan, H. Oigawa and A. Koma: Jpn. J. Appl. Phys. **27** (1988) L2367.

[33] K. Sato, M. Sakata and H. Ikoma: Jpn. J. Appl. Phys. **32** (1993) 3354.

[34] C. J. Sandroff, R. N. Nottenburg, J. -C. Bischoff and R. Bhat: Appl. Phys. Lett. **51** (1987) 33.

[35] K. C. Hwang and S. S. Li: J. Appl. Phys. **67** (1990) 2162.

[36] M. J. Chester, T. Jach and J. A. Dagata: J. Vac. Sci. & Technol. A**11** (1993) 474.

[37] Y. Hashimoto, J. Sakurai, I. Minemura and K. Ito: Jpn. J. Appl. Phys. **34** (1995) 3075.

[38] F. Capasso and G. F. Williams: J. Electrochem. Soc. **129** (1982) 821.

[39] A. Callegari, D. Lacey, D. A. Buchanan, E. Latta, M. Gasser and A. Paccagnella: *Proc. Int. Symp. GaAs and Related Compounds, Karuizawa, 1989* (IOP Publishing, Bristol, 1990) Inst. Phys. Conf. Ser., No. 106, Chap. 6, p. 399.

[40] A. Tamura, M. Kitagawa and S. Nambu: *Proc. Int. Symp. GaAs and Related Compounds, Jersey, 1990* (IOP Publishing, Bristol, 1990) Inst. Phys. Conf. Ser., No. 112, Chap. 5, p. 299.

[41] C. Y. Wu and M. S. Lin: J. Appl. Phys. **60** (1986) 2050.

[42] L. A. DeLouise: J. Vac. Sci. & Technol. A**10** (1992) 1637.

[43] J. S. Herman and F. L. Terry, Jr.: Appl. Phys. Lett. **60** (1992) 716.

[44] N. Yoshida, S. Chichibu, T. Akane, M. Totsuka, H. Uji, S. Matsumoto and H. Higuchi: Appl. Phys. Lett. **63** (1993) 3035.

[45] T. Sugino, T. Yamada and J. Shirafuji: Jpn. J. Appl. Phys. **29** (1990) L864.

[46] T. Harada, H. Yoshida, K. Yasui and T. Akahane: Tech. Report of Inst.

Electron., Inform. and Commun. Eng., Vol. 95, No. 284, CPM95-71 (1995) p. 7 [in Japanese].

Chapter 5 Plasma Oxidation of Si

5.1 *Background*

SiO_2 is one of the most important materials in Si LSI technology, employed as the gate insulator, interlayer insulator, etc. Recent development of scaled floating-gate memories such as advanced electrically erasable programmable read-only memories (EEPROMs) and flash memories urgently requires the control of ultrathin-oxide thickness because of the scaling rule. For example, EEPROM tunnel oxide requires reliable thin dielectrics of the thickness smaller than 100 Å. Rapid thermal oxidation is one of the promising candidates for forming the ultrathin oxide. For example, Si oxidation technique in N_2O ambient by rapid thermal process (RTP) has recently attracted much attention from the viewpoint of both industrial application and physical interest [1,2]. It is well-known that N atoms accumulate at the SiO_2/Si interface in the case of RTP process using N_2O. It was reported that the self-limiting mechanism in the oxide growth is brought about by the accumulation of N atoms at the interface, namely, that the accumulating N atoms hinder the oxide growth [3,4]. On the other hand, Kuiper *et al.* [5] found that the accumulating N atoms are not sufficient to stop the progress of the oxidation, although it retards the oxide growth.

Thermal oxidation is, however, brings about the increase in stacking faults and in the diffusion of implanted impurities although the RTP process is often employed as above mentioned. Plasma oxidation is one of the attractive alternative candidates for decreasing the process temperature and for

decreasing the above-mentioned problems. Local oxidation of Si (LOCOS) is a typical example of applying the plasma oxidation to Si LSI technology. The plasma oxidation at low temperature using unbiased Si substrates also has the possibility to control the ultrathin-oxide thickness because of its low oxidation rate. It is very attractive from the viewpoint of decreasing the process temperature to apply N_2O-plasma oxidation technique, which has the possibility to yield improved electrical properties, to formation of ultrathin SiO_2 on Si. After the first attempt of the N_2O-plasma oxidation of Si described in this chapter, excellent oxide-breakdown properties were also reported by other group for the N_2O-plasma oxidized Si [6,7].

The *Pb* center which is a well-known defect at the SiO_2/(111)Si interface is also the problems to be solved. However, not so many ESR studies have been carried out on the *Pb* center in the plasma-oxidized (111)Si [8] although the nature of the *Pb* center has been investigated in detail using electron spin resonance (ESR) for the thermal oxide formed on (111)Si [9-11].

In this chapter detailed physics and kinetics of O_2- and N_2O-plasma oxidation, such as the oxide-growth rate and the oxide-growth mode is discussed based on the experimental results obtained by X-ray photoelectron spectroscopy (XPS) and ellipsometry. The accumulation process of N atoms at or near the SiO_2/Si interface for N_2O-plasma oxidized Si is shown. ESR study on *Pb* center is also presented.

5.2 *Oxidation process*

O_2- or N_2O-plasma oxidation process for (100) and (111) Si will be discussed in this section. All the samples except for those formed on (100)Si

using an N_2O plasma were characterized using XPS. All the observed Si 2*p* spectra showed both the signal due to the oxide and that due to the underlayer Si substrate. Judging from the difference between the binding energy (BE) for Si 2*p* signal due to the Si substrate and the BE for that due to the oxide, the stoichiometric SiO_2 is formed by the plasma oxidation regardless of the substrate orientation, the oxidation time or the type of the oxidant.

The oxide thickness evaluated by the ellipsometry against the O_2- or N_2O-plasma oxidation time is shown in Fig. 5.1. The average error of the thickness due to the measurement system was estimated to be smaller than ± 5 % for more than 30 samples. The rapid oxidation is found in the early stage, while the oxide-growth rate lowers after the oxidation for 10 min. This tendency is similar to that observed NH_3-plasma nitridation of (100)GaAs, as shown in Fig. 4.10. Saturation in the oxide growth seems to be observed with the oxidation for 120 min. As can be seen from Fig. 5.1, the oxide growth rate for long oxidation time in the N_2O-plasma oxidation appears to be smaller than that in O_2-plasma oxidation. For N_2O-plasma oxidized Si, N-atom accumulation at the SiO_2/Si interface has been found as shown in § 5.3. N atoms accumulated at the SiO_2/Si interface have been known to retard the oxidation in the case of the rapid thermal oxidation of Si in an N_2O ambient [3-5] as mentioned in § 5.1. It is possible that the increased N atoms accumulated at the SiO_2/Si interface makes the smaller oxide-growth rate in the N_2O-plasma oxidation. Kuroki *et al.* [12,13] observed using the real-time ellipsometry that the oxide-growth rate in (111)Si is larger than that in (100)Si for the rf plasma oxidation. Also in the thermal oxidation, the same tendency was found by Ohmi *et al.* [14]. However, no clear evidence is shown in Fig. 5.1 that the oxide-growth rate on (111)Si is larger than that on (100)Si both in the cases using O_2 plasma and

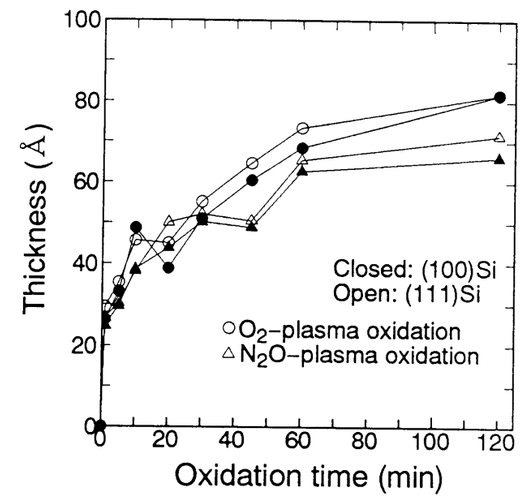

Fig. 5.1. Oxidation-time dependence of the oxide thickness for (111) and (100)Si oxidized using O_2 or N_2O plasma.

N_2O plasma, taking consideration into the above-mentioned errors.

5.3 *N accumulation at the SiO_2/Si interface*

It is found both by angle-dependent XPS (ADXPS) and XPS with Ar ion sputtering that in N_2O-plasma oxidation N atoms accumulate at or near the SiO_2/Si interface. The BE of N 1*s* is 397.5 eV, showing that N is bonded to Si, not to O. The accumulation process of N during N_2O-plasma oxidation is shown in Fig. 5.2. The ordinate and the abscissa in Fig. 5.2 show the N 1*s* XPS intensity and the Ar ion sputtering time during XPS measurements, respectively. Therefore, Fig. 5.2 roughly represents the depth profiles of N in the samples. It is clearly found in Fig. 5.2 that the distribution of N shows the symmetric form and that its peak position moves from the sample surface into the bulk region accompanied with the oxide growth. Therefore it is confirmed that the N atoms always accumulate toward the SiO_2/Si interface.

Figure 5.3 shows the behavior of N and O contents in the oxide or at the SiO_2/Si interface against the N_2O-plasma-oxidation time. N and O contents were determined by integrating the depth profile of N 1*s* and O 1*s* XPS intensity, respectively. Both of N and O contents for the sample oxidized for 1 min are normalized to 1. Therefore the relative comparison between N and O contents in Fig. 5.3 makes no sense. It is found from both Figs. 5.1 and 5.3 that the incorporation of O roughly reflects the increment of the oxide thickness. N content in the sample is thought to be determined by the balance between incorporation and release of N atoms, because N atoms are taken into the sample even through the oxide as Fukuda *et al.* reported in the case of RTP of SiO_2 in N_2O ambient [2]. It is elucidated from Fig. 5.3

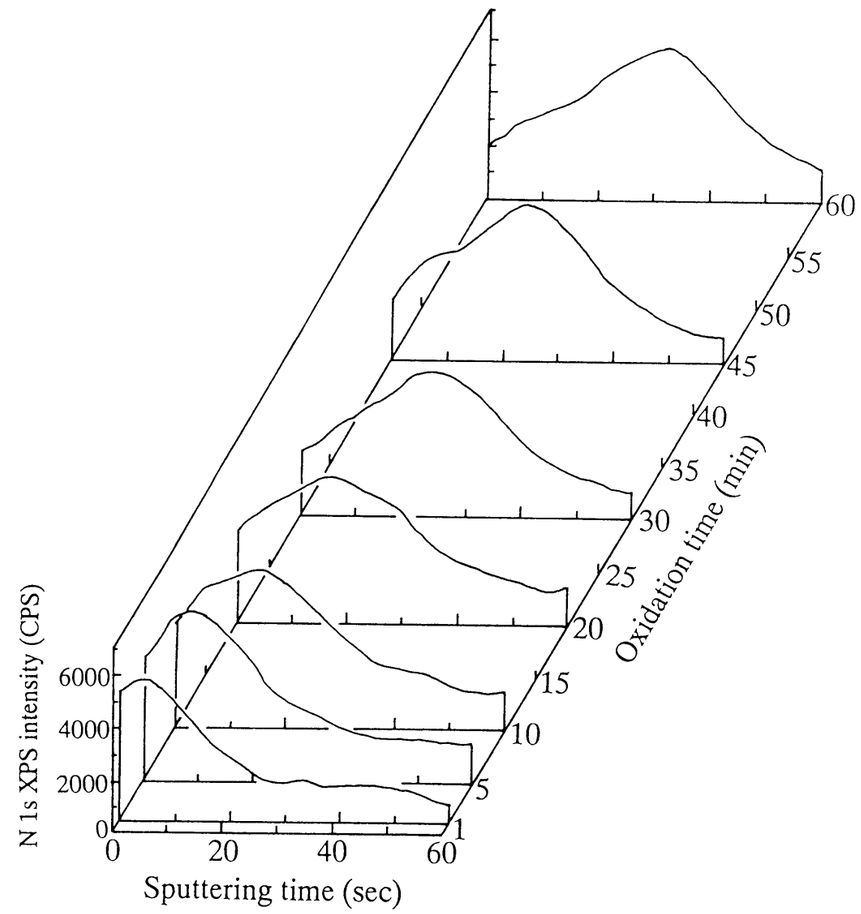

Fig. 5.2. N 1*s* XPS intensities against the sputtering time during XPS measurements for samples oxidized for various times.

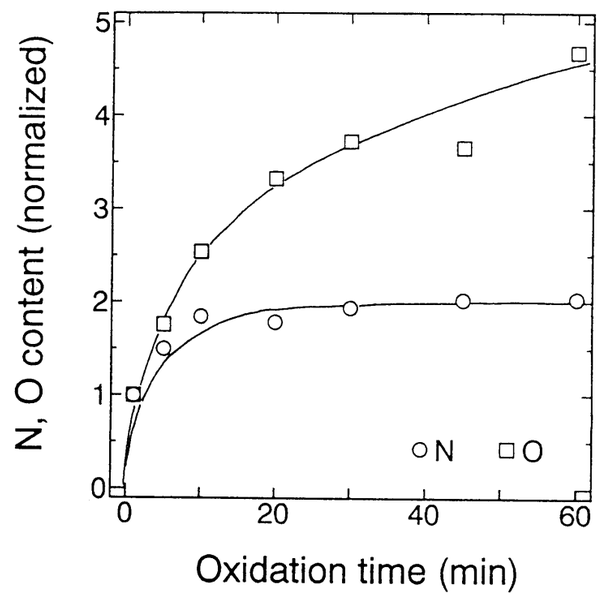

Fig. 5.3. Oxidation time dependence of incorporated N (○) and O (□) contents. Solid lines are shown to guide the eye.

that the incorporated N content increases only at the early stage of the oxidation and is almost unchanged with the oxidation for longer than 10 min. On the other hand, the incorporated O content, namely the SiO_2 thickness, continues to increase during the oxidation for 60 min. The experimental fact that the difference between incorporated and released N atoms is constant suggests that the number of the possible sites bonded to N at or near the SiO_2/Si interface is finite and most of the sites are occupied through the oxidation for 10 min. It is revealed from the above-mentioned results that it is easy for N atoms to exist at or near the SiO_2/Si interface, but difficult to exist in the bulk oxide. However, the mechanism for the accumulation of N atoms at the interface remains as a problem to be solved.

5.4 *Oxide-growth mode*

The oxide-growth mode in the plasma oxidation is discussed based on the results obtained using XPS. Figures 5.4 (a), (b) and (c) show the XPS intensity ratio against the oxide thickness estimated by the ellipsometry for (111)Si oxidized using O_2 plasma, for (111)Si oxidized using N_2O plasma and for (100)Si oxidized using O_2 plasma, respectively. Open circles in Fig. 5.4 show the ratio of the intensity of Si 2*p* signal due to Si substrate to the total intensity of Si 2*p*. Closed ones show the ratio of the intensity of Si 2*p* signal due to SiO_2 to the total intensity of Si 2*p*. Thus the sum of the value shown by a open circle and that shown by a closed one is unity. The Si 2*p* XPS signal due to Si decreases and that due to SiO_2 increases with the increase in SiO_2 thickness. The oxidation of (111)Si using O_2 plasma, that of (111)Si using N_2O plasma and that of (100)Si using O_2 plasma are alike in the

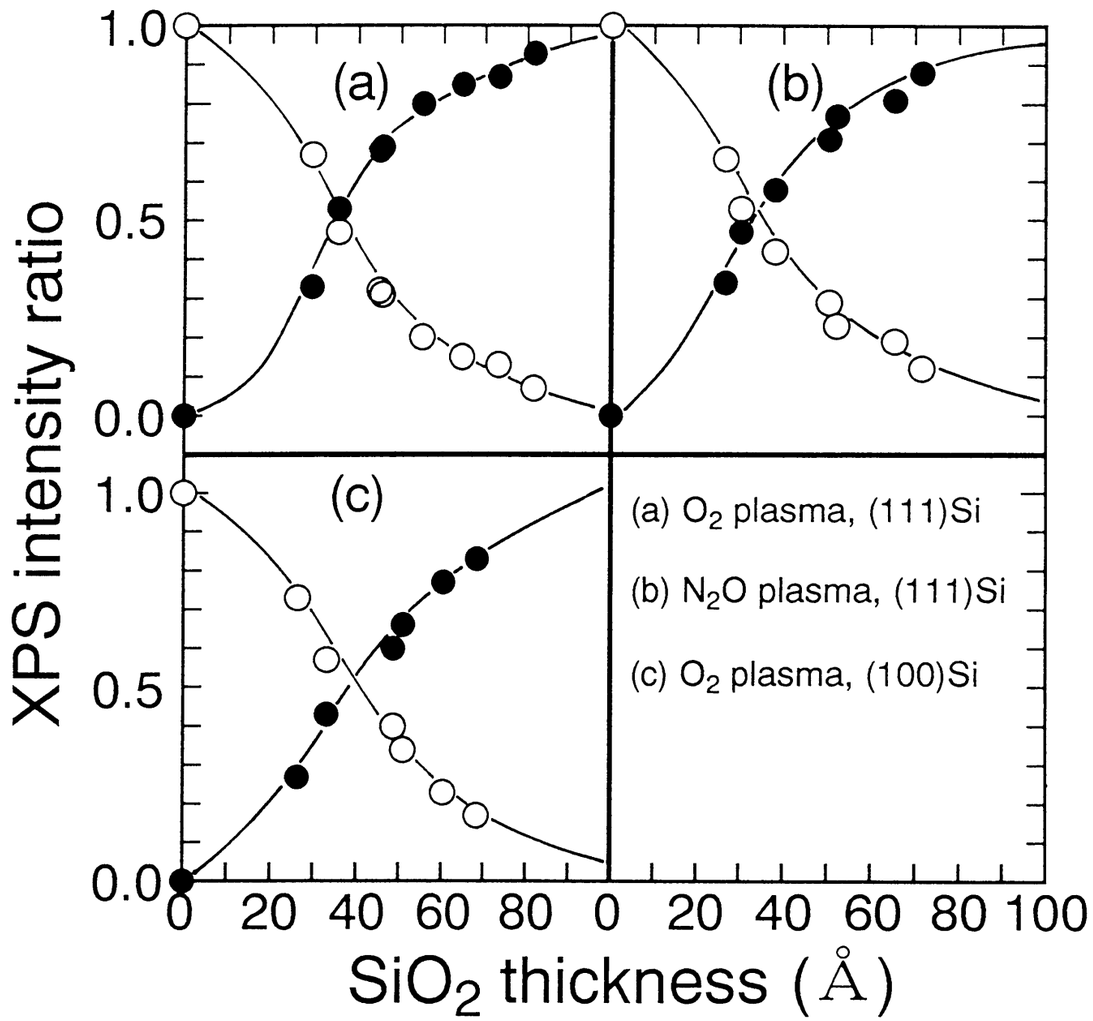

Fig. 5.4. XPS intensity ratio against the oxide thickness for (a) (111)Si oxidized using O_2 plasma, (b) (111)Si oxidized using N_2O plasma, (c) (100)Si oxidized using O_2 plasma, respectively. The definition of the XPS intensity ratio and the meanings shown by open and closed circles are given in the text. Solid lines are shown to guide the eye.

signal-intensity behavior against SiO_2 thickness. The XPS signal intensity due to Si, I_{Si}, exponentially decreases with the oxide growth as follows [15] if the ideal two-dimensional growth of SiO_2 occurs.

$$\frac{I_{SiO_2}}{I_{Si}} = \frac{\rho_{SiO_2}\lambda_{SiO_2}}{\rho_{Si}\lambda_{Si}}\left(\exp\left(\frac{d_{SiO_2}}{\lambda_{Si}\sin\theta}\right)-1\right) \tag{5.1}$$

Meanings of the symbols in eq. (5.1) are shown in Table 5.1. The photoelectron escape depth in SiO_2, λ_{SiO_2}, estimated using eq. (5.1) is not larger than the ideal value of 30 Å. If SiO_2 layer grows with a three-dimensional growth, the photoelectron escape depth in SiO_2 should be larger than ideal value. Therefore these results suggest that the oxide-growth mode on Si is a two-dimensional growth regardless of the substrate orientation or the type of the oxidant.

5.5 *Electron spin resonance study on SiO_2/Si interface*

O_2- or N_2O-plasma oxidized (111)Si was characterized using ESR. ESR spectra in the as-grown sample oxidized using N_2O-plasma for 30 min were shown in Fig. 5.5. No remarkable change in the shape of ESR spectra were observed with the oxidation time over the range from 1 min to 60 min or the type of the oxidant. Figures 5.5 (a) and 5.5 (b) show the ESR spectra observed with the [111] axis parallel to the static magnetic field ([111] $\parallel$ H) and with the [111] axis perpendicular to the static magnetic field ([111] $\perp$ H), respectively. These two spectra are shown with the same scale. The

Table 5.1. Meanings of the symbols in eq. (5.1).

I_{SiO_2}	Intensity of Si 2*p* XPS signal due to SiO_2
I_{Si}	Intensity of Si 2*p* XPS signal due to Si
ρ_{SiO_2}	Number of Si atoms in SiO_2 per unit volume
ρ_{Si}	Number of Si atoms in Si per unit volume
λ_{SiO_2}	Photoelectron escape depth in SiO_2
λ_{Si}	Photoelectron escape depth in Si
d_{SiO_2}	SiO_2-layer thickness
θ	Photoelectron take-off angle

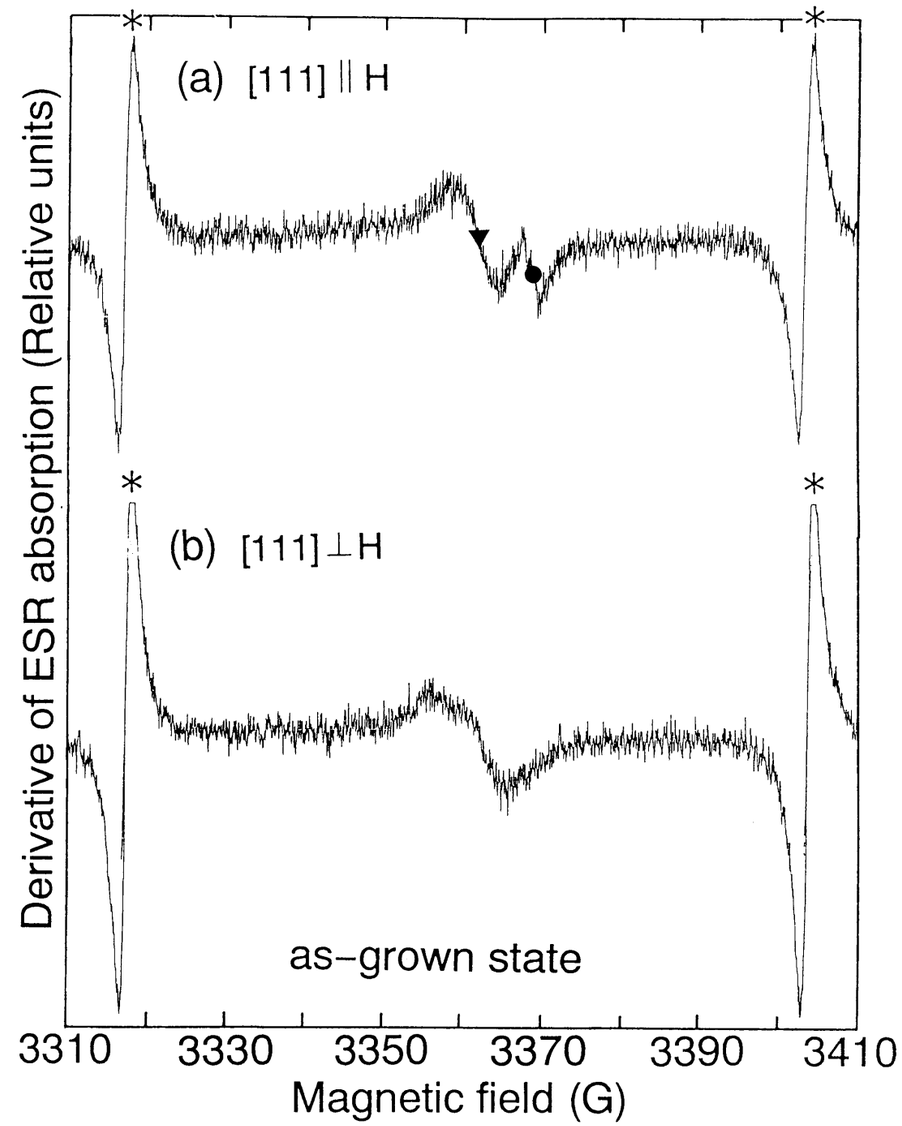

Fig. 5.5. ESR spectra observed (a) with the [111] axis parallel to the static magnetic field ([111] || H) and (b) with the [111] axis perpendicular to the static magnetic field ([111] ⊥ H) for the as-grown sample oxidized using N_2O-plasma for 30 min. Both the spectra are shown with the same scale. Circular symbol and triangular symbol represent the signal due to the *Pb* center and that due to the *D* center, respectively. Asterisk symbols represent the hyperfine structure due to the Mn^{2+} marker in the MgO powder.

difference between the two spectra shown in Figs. 5.5 (a) and 5.5 (b) shows that the ESR centers have the anisotropy against the magnetic field. The signal separation of the spectrum shown in Fig. 5.5 (a) reveals the existence of two kinds of ESR centers: one center shown by a circular symbol has the *g*-value of 2.0017 and the linewidth of 2.2 G, and the other center shown by a triangular symbol has the *g*-value of 2.0058 and the linewidth of 5.7 G. It is also revealed that the former signal has the anisotropy against the magnetic field, while the latter one has no anisotropy. Judging from the *g*-value and the anisotropy against the magnetic field, the former signal is believed to originate from the so-called *Pb* center, which is the Si dangling bond (DB) back-bonded to three Si atoms at the SiO2/(111)Si interface. On the other hand, the latter signal is supposed to originate from ESR centers which resemble Si DBs in amorphous Si. Hereafter, such ESR centers are named *D* center in this article for convenience. It was also confirmed that both the *Pb* center and the *D* center are produced by the plasma oxidation because no ESR signals due to both centers are observed in (111)Si just after the aqueous treatment with HF solution mentioned in § 2.1.4. The total spin density per area and the ratio of the *Pb*-center density to the total spin density were $2 \times 10^{13} - 4 \times 10^{13}$ cm^{-2} and 6 - 14 % for oxidation time from 1 min to 60 min regardless of the type of the oxidant. The *Pb*-center density per area is shown in Fig. 5.6 for these samples as a function of the oxidation time. Lower *Pb*-center density by about 30 % is obtained using N2O plasma than using O2 plasma after the oxidation for longer than 20 min. On the other hand, no clear dependence of the *D*-center density per area on the oxidation time or the type of the oxidant is observed, as shown in Fig. 5.7. Both the *g*-values and linewidths for the *Pb* center and those for the *D* center were also roughly independent of the oxidation time.

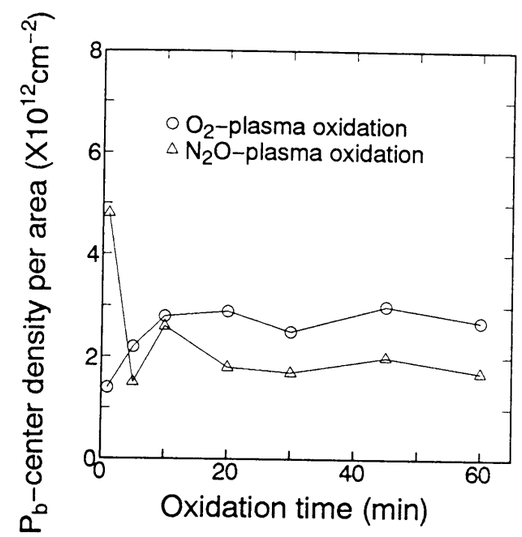

Fig. 5.6. *Pb*-center density per area against the oxidation time.

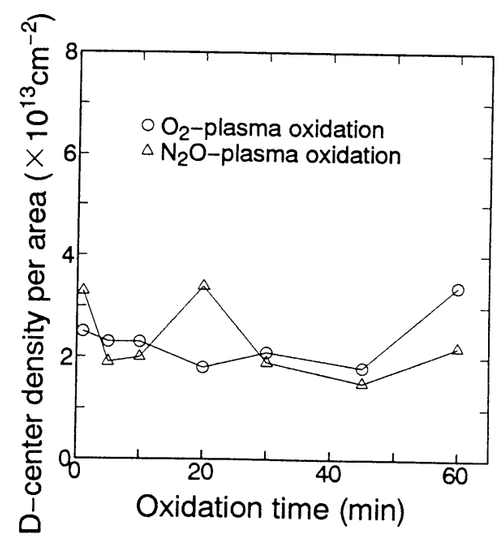

Fig. 5.7. *D*-center density per area against the oxidation time.

The sample whose ESR spectra in the as-grown state are shown in Fig. 5.5 was annealed at 800 ℃ for 2 h in a vacuum of 3×10^{-3} Pa. It was confirmed that no oxidation due to the residual O_2 or H_2O in the vacuum occurs during the annealing because no increase in the oxide thickness after the annealing was observed using the ellipsometry. ESR spectra after the annealing are shown in Fig. 5.8. The ESR spectra in Figs. 5.8 (a) and 5.8 (b) were observed with [111] ∥ H and with [111] ⊥ H, respectively. All of these two spectra and the spectra shown in Figs. 5.5 (a) and 5.5 (b) are shown with the same scale. The circular symbols and the triangular symbol represent the signal due to the *Pb* center and that due to the *D* center, respectively, as in Fig. 5.5. After the annealing, the signal due to the *Pb* center has the *g*-value of 2.0019 in the case observed with [111] ∥ H and has the *g*-value of 2.0090 in the case observed with [111] ⊥ H. The total spin density per area, the *Pb*-center density per area and the *D*-center density per area in the as-grown state and in the annealed state are summarized in Table 5.2. The *Pb*-center density was increased with the annealing, although both the total spin density and the *D*-center density were decreased with the annealing. Both of the ESR spectra observed with [111] ∥ H and with [111] ⊥ H after the annealing closely resemble those for (111)Si with the native oxide recently reported by Yokogawa *et al.* [16] both in the shape of the spectra and in the ratio of the *Pb*-center density to the *D*-center density. These facts suggest that the SiO_2/(111)Si interface formed by the plasma oxidation with the successive annealing is equivalent to the interface between native oxide and (111)Si although the *Pb*-center density is increased during the annealing with the structural relaxation. It is also noticeable that the *Pb*-center density in the above-mentioned sample even after the annealing is comparable to that in the SiO_2/(111)Si interface formed by a thermal oxidation [17].

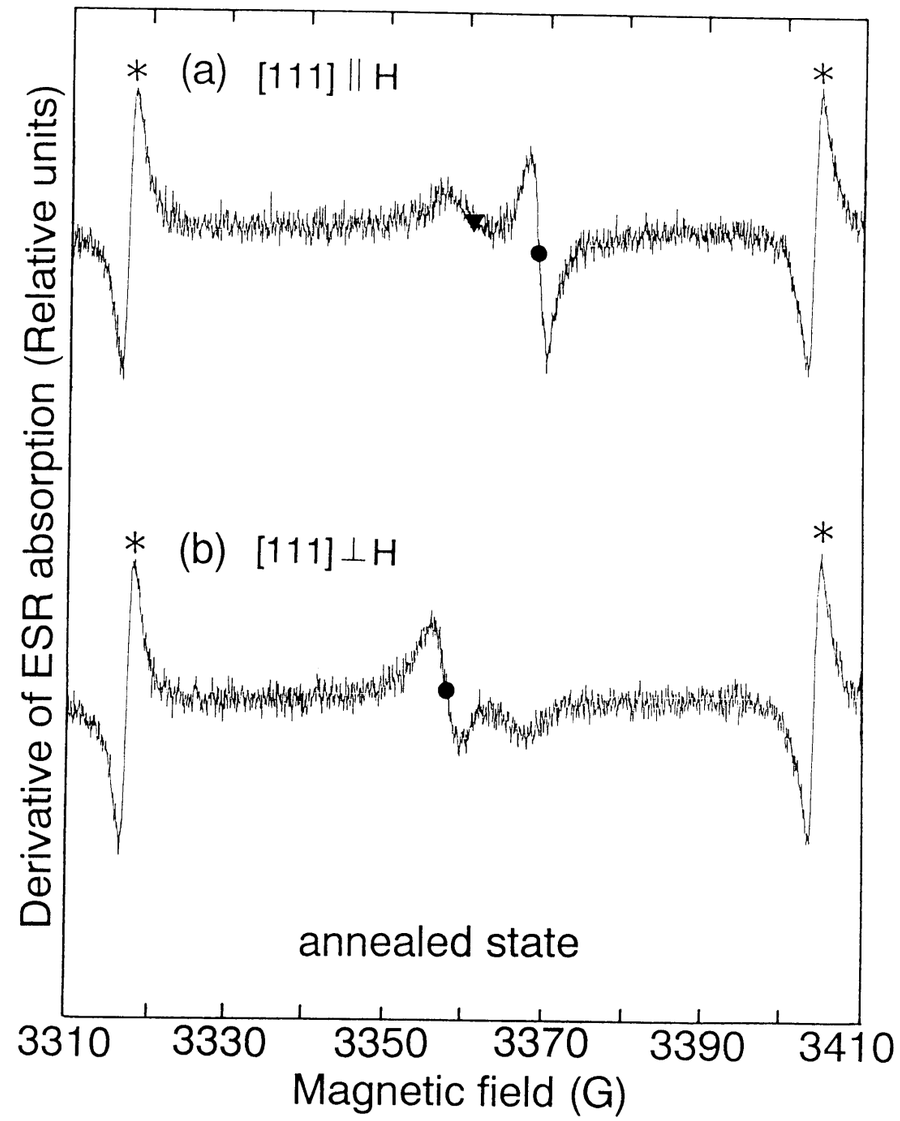

Fig. 5.8. ESR spectra observed (a) with the [111] axis parallel to the static magnetic field ([111] ∥ H) and (b) with the [111] axis perpendicular to the static magnetic field ([111] ⊥ H) for the sample oxidized using N_2O-plasma for 30 min and successively annealed at 800 ℃ for 2 h in a vacuum. Both the spectra in Fig. 5.8 and those in Fig. 5.5 are shown with the same scale. Circular symbols and triangular symbol represent the signal due to the *Pb* center and that due to the *D* center, respectively. Asterisk symbols represent the hyperfine structure due to the Mn^{2+} marker in the MgO powder.

Table 5.2. The total spin density per area, the *Pb*-center density per area and the *D*-center density per area in the as-grown state and in the annealed state for (111)Si oxidized using N_2O plasma for 30 min.

	Total spin density per area (cm^{-2})	*Pb*-center density per area (cm^{-2})	*D*-center density per area (cm^{-2})
as-grown state	2.1×10^{13}	1.7×10^{12}	1.9×10^{13}
annealed state	1.8×10^{13}	7.0×10^{12}	1.1×10^{13}

5.6 *Summary*

Plasma oxidation of (100) and (111)Si on the anode electrode was carried out using O_2 plasma or N_2O plasma. The rapid oxide-growth in the early stage is observed irrespective of the substrate orientation and the type of the oxidant. Accumulation of N atoms at or near the SiO_2/Si interface was observed by XPS for the N_2O-plasma oxidation of Si in the same way as in the case of RTP of Si in N_2O ambient. The increase in the incorporated N content is observed only at the early stage of the oxidation, and the content of accumulating N remains constant with the oxidation for longer time. It is supposed that the oxide-growth mode on Si by the plasma oxidation is the two-dimensional growth regardless of the substrate orientation or the type of the oxidant. ESR observation reveals that at the SiO_2/(111)Si interface formed by the plasma oxidation there are Si DBs similar to those in amorphous Si in addition to *Pb* center. The *Pb*-center density at the SiO_2/(111)Si interface formed by the N_2O-plasma oxidation is comparable to that formed by a thermal oxidation.

References in Chapter 5

[1] H. Hwang, W. Ting, B. Maiti, D. -L. Kwong and J. Lee: Appl. Phys. Lett. **57** (1990) 1010.

[2] H. Fukuda, T. Arakawa and S. Ohno: Jpn. J. Appl. Phys. **29** (1990) L2333.

[3] W. Ting, H. Hwang, J. Lee and D. L. Kwong: J. Appl. Phys. **70** (1991) 1072.

[4] S. Dimitrijev, D. Sweatman and H. B. Harrison: Appl. Phys. Lett. **62** (1993) 1539.

[5] A. E. T. Kuiper, H. G. Pomp, P. M. Asveld, W. A. Bik and F. H. P. M. Habraken: Appl. Phys. Lett. **61** (1992) 1031.

[6] P. C. Chen, K. Y. J. Hsu, H. L. Hwang and J. Y. Lin: J. Appl. Phys. **76** (1994) 5508.

[7] P. C. Chen, K. Y. J. Hsu, J. Y. Lin and H. L. Hwang: Jpn. J. Appl. Phys. **34** (1995) 973.

[8] V. Q. Ho and T. Sugano: IEEE Trans. Electron Devices **ED-28** (1981) 1060.

[9] Y. Nishi: Jpn. J. Appl. Phys. **10** (1971) 52.

[10] P. J. Caplan, E. H. Poindexter, B. E. Deal and R. R. Razouk: J. Appl. Phys. **50** (1979) 5847.

[11] A. Stesmans: Phys. Rev. B**48** (1993) 2418.

[12] H. Kuroki, T. Kawabe and M. Kitajima: Solid State Commun. **88** (1993) 785.

[13] H. Kuroki, K. G. Nakamura, I. Kamioka, T. Kawabe and M. Kitajima: J. Vac. Sci. & Technol. A**12** (1994) 1431.

[14] T. Ohmi, K. Matsumoto, K. Nakamura, K. Makihara, J. Takano and K. Yamamoto: Appl. Phys. Lett. **62** (1993) 405.

[15] A. Ishizaka, S. Iwata and Y. Kamigaki: Surf. Sci. **84** (1979) 355.

[16] K. Yokogawa and T. Mizutani: Jpn. J. Appl. Phys. **32** (1993) L635.

[17] K. Awazu, H. Kawazoe, T. Ando and K. Watanabe: J. Appl. Phys. **70** (1991) 2979.

Chapter 6 Conclusions

Interface-control technique of semiconductors is studied in prospect of integrated devices with layered structure composed of ferroelectric oxide films or Ⅲ - Ⅴ nitrides and conventional semiconductors such as Si and GaAs. SiO_2/Si interface control is also important for establishing the well-ordered ultrathin-oxide formation technique. In this article, various interface-control techniques have been presented with three examples. Significance and future prospects obtained in each chapter are separately shown below, while detailed results obtained in these three examples were already summarized in each chapter.

In Chap. 3, it is shown that the interface between $Pb(Zr,Ti)O_3$ (PZT) films and GaAs or Si substrate is well controlled by employing the MgO buffer layer. MgO buffer layer acts as the template layer for relaxing the lattice mismatch with four units of MgO and three units of GaAs or Si, as the diffusion barrier at the interface and as the capping layer for preventing both the vaporization of As from GaAs and the oxidation of Si during the deposition of PZT films. Highly oriented PZT films were obtained because of these excellent buffer-layer characteristics of MgO.

In Chap. 4, the NH_3-plasma-nitridation process of GaAs is clarified using X-ray photoelectron spectroscopy (XPS) with changing the photoelectron take-off angle. Since the nitridation of GaAs is recently often employed for the buffer-layer formation technique between GaN films and GaAs substrate, this clarification will certainly contribute to growing high-quality cubic β-GaN films on GaAs with establishing their

interface-control technique.

In Chap. 5, the possibility of controlling the ultrathin oxide thickness by the SiO_2/Si interface control is presented in the plasma-oxidation of Si at low temperature in prospect of developing scaling floating-gate memories. The oxide-growth rate and the oxide growth mode in the early stage of the oxidation gives the information on the SiO_2/Si interface-control technique. N accumulation at their interface observed for the N_2O-plasma oxidation also has the possibility to contribute to controlling the ultrathin oxide thickness by lowering the oxide-growth rate.

Recent development in electronic devices requires the more complicated device structures. Since most of them consist of layered thin-film structure, those working on thin-film electronic materials are required to fabricate highly controllable, sophisticated and artificial structures such as superlattices and quantum dots, etc. If the interface-control techniques presented in this article will contribute, even slightly, to these newly developing next-generation electronic devices, that is an unexpected gladness of the author.

Acknowledgements

The author expresses his sincere appreciation to Professor Tatsuo Shimizu for his valuable suggestions, stimulating discussions and encouragement throughout this study. He also would like to acknowledge Professor Minoru Kumeda and Dr. Akiharu Morimoto for their valuable suggestions and discussions.

The author expresses his appreciation to Mr. Toshiharu Minamikawa of the Industrial Research Institute of Ishikawa Prefecture, Mr. Yasuto Yonezawa of the Industrial Research Institute of Ishikawa Prefecture, Mr. Takanori Nakamura of the Murata Mfg. Co., Ltd., Mr. Yasuhiro Yamanaka, now with the Matsushita Electronics Corporation, and Mr. Mitsutoshi Tazoe for their collaboration in this study. Most of measurements yielding important results in this study were carried out by them. He also expresses his appreciation to Ms. Kazuko Matsuda, Mr. Satoshi Usui and Mr. Hideki Shigeno for their fruitful discussions on pulsed laser ablation.

The author would like to acknowledge Professor Tomonobu Hata of Kanazawa University and Professor Ichiro Watanabe of Kanazawa University for their critical reading of this thesis.

The author is grateful to Mr. Katsuroh Nagai for his technical assistance and Dr. Shigeru Otsubo of the Shibuya Kogyo Co., Ltd. for the maintenance of ArF excimer laser.

The author is also grateful to Dr. Keiichi Nashimoto of the Materials Research Laboratory, Fuji Xerox Co., Ltd. for his collaboration whose results were shown in § 3.2, Dr. David K. Fork of the Xerox Palo Alto Research

Center for ϕ -scan measurements shown in § 3.2, Mr. Masao Watanabe of the Materials Research Laboratory, Fuji Xerox Co., Ltd. for the use of the electron-beam evaporation system shown in § 3.2, Dr. Akinori Inoue of the Materials Research Laboratory, Fuji Xerox Co., Ltd. for his encouragement in the study shown in § 3.2, Dr. Michio Sato of the NTT Basic Research Laboratories and Mr. Satoshi Kodama of the Hokkaido University for their fruitful suggestions and discussions in the study shown in Chap. 4. He also would like to acknowledge Dr. Toshiki Makimoto of the NTT Basic Research Laboratories and Dr. Kunihiko Uwai of the NTT Basic Research Laboratories for sending him the article cited as Refs. 25-27 in Chap. 4 before publication, Professor Akio Yamamoto of the Fukui University for sending him the article cited as Ref. 20 in Chap. 4 before publication and Mr. Hiroki Sugiyama of the NTT LSI Laboratories for sending him the article cited as Ref. 21 in Chap. 4 before publication and their fruitful discussions.

Thanks are also due to Shibuya Kogyo Co., Ltd. for supplying the ArF excimer laser and Murata Mfg. Co., Ltd. for Auger electron spectroscopy measurement.

The work shown in § 3.3-3.5 was in part supported by the Grant-in-Aid for Development Scientific Research No. 07555499 from the Ministry of Education, Science, Sports and Culture of Japan, the Grant-in-Aid for Scientific Research (C) No. 06650010 from the Ministry of Education, Science, Sports and Culture of Japan, the Murata Science Foundation, the Akai Foundation and Murata Mfg. Co., Ltd.

Publication Lists

A) List of publications relating to the thesis

1) Atsushi Masuda and Keiichi Nashimoto
Orientation of MgO thin films on Si(100) and GaAs(100) prepared by electron-beam evaporation
Jpn. J. Appl. Phys. Part 2 **33** (6A), L793-L796 (1994). (June, 1994)

2) Atsushi Masuda, Yasuto Yonezawa, Akiharu Morimoto and Tatsuo Shimizu
Surface nitridation process of (100) GaAs by NH_3-plasma treatment with planar magnetic field
Extended Abstracts of the 1994 International Conference on Solid State Devices and Materials, Yokohama, 1994 (Business Center for Academic Societies Japan, Tokyo, 1994) pp. 193-195. (August, 1994)

3) Atsushi Masuda, Yasuto Yonezawa, Akiharu Morimoto, Minoru Kumeda and Tatsuo Shimizu
Ultrathin SiO_2 films on Si formed by N_2O-plasma oxidation technique
Appl. Surf. Sci. **81** (3), 277-280 (1994). (November, 1994)

4) Atsushi Masuda, Yasuto Yonezawa, Akiharu Morimoto and Tatsuo Shimizu
NH_3-plasma-nitridation process of (100) GaAs surface observed by angle-dependent X-ray photoelectron spectroscopy
Jpn. J. Appl. Phys. Part 1 **34** (2B), 1075-1079 (1995). (February, 1995)

5) Atsushi Masuda, Yasuhiro Yamanaka, Mitsutoshi Tazoe, Yasuto Yonezawa, Akiharu Morimoto and Tatsuo Shimizu
Highly oriented $Pb(Zr,Ti)O_3$ thin films prepared by pulsed laser ablation on GaAs and Si substrates with MgO buffer Layer
Jpn. J. Appl. Phys. Part 1 **34** (9B), 5154-5157 (1995). (September, 1995)

6) Atsushi Masuda, Yasuhiro Yamanaka, Mitsutoshi Tazoe, Takanori Nakamura, Akiharu Morimoto and Tatsuo Shimizu
Preparation and crystallographic characterizations of highly oriented $Pb(Zr_{0.52}Ti_{0.48})O_3$ films and MgO buffer layers on (100)GaAs and (100)Si by pulsed laser ablation
J. Cryst. Growth **158** (1-2), 84-88 (1996). (January, 1996)

7) Atsushi Masuda, Yasuto Yonezawa, Akiharu Morimoto and Tatsuo Shimizu
X-ray photoelectron spectroscopy of GaN layer formed on GaAs by NH_3-plasma nitridation and successive excimer-laser irradiation
Inst. Phys. Conf. Ser. (1996). (Accepted and now in press)

8) Atsushi Masuda, Yasuto Yonezawa, Akiharu Morimoto, Minoru Kumeda and Tatsuo Shimizu
X-ray photoelectron spectroscopy and electron spin resonance studies on O_2- and N_2O-plasma oxidation of silicon
Mater. Sci. Eng. B (1996). (Accepted and now in press)

b) List of other publications

1) Atsushi Masuda, Minoru Kumeda and Tatsuo Shimizu
Relationship between photodarkening and light-induced ESR in amorphous Ge-S films alloyed with lead
Jpn. J. Appl. Phys. Part 2 **30** (6B), L1075-L1078 (1991). (June, 1991)

2) Atsushi Masuda, Minoru Kumeda, Akiharu Morimoto and Tatsuo Shimizu
Light-induced ESR and disappearance of photodarkening in amorphous Ge-S films alloyed with lead
J. Non-Cryst. Solids **137&138** pt. 2, 985-988 (1991). (December, 1991)

3) Atsushi Masuda, Akiharu Morimoto, Minoru Kumeda, Tatsuo Shimizu, Yasuto Yonezawa and Toshiharu Minamikawa
Novel oxidation process of hydrogenated amorphous silicon utilizing nitrous oxide plasma
Appl. Phys. Lett. **61** (7), 816-818 (1992). (August, 1992)

4) Atsushi Masuda, Iwao Fukushi, Yasuto Yonezawa, Toshiharu Minamikawa, Akiharu Morimoto, Minoru Kumeda and Tatsuo Shimizu
Spectroscopic study on N_2O-plasma oxidation of hydrogenated amorphous silicon and behavior of nitrogen
Jpn. J. Appl. Phys. Part 1 **32** (6A), 2794-2802 (1993). (June, 1993)

5) Atsushi Masuda, Ken-ichi Itoh, Jiang-Huai Zhou, Minoru Kumeda and Tatsuo Shimizu
Relationship between electrical conductivity and charged-dangling-bond density in nitrogen- and phosphorus-doped hydrogenated amorphous silicon
Jpn. J. Appl. Phys. Part 2 **33** (9B), L1295-L1297 (1994). (September, 1994)

6) Koichi Shimakawa, Takeharu Kato, Koji Hayashi, Atsushi Masuda, Minoru Kumeda and Tatsuo Shimizu
Correlation between a.c. transport and electron spin resonance in amorphous Ge-S films alloyed with lead
Philos. Mag. B**70** (5), 1035-1044 (1994). (November, 1994)

7) Hoonkee Min, Iwao Fukushi, Atsushi Masuda, Akiharu Morimoto, Minoru Kumeda and Tatsuo Shimizu
Interfacial neutral- and charged-dangling-bond densities between hydrogenated amorphous silicon and hydrogenated amorphous silicon nitride in top nitride and bottom nitride structures
Appl. Phys. Lett. **66** (20), 2718-2720 (1995). (May, 1995)

8) Atsushi Masuda, Kazuko Matsuda, Yasuto Yonezawa, Akiharu Morimoto and Tatsuo Shimizu
Mechanism of stoichiometric deposition of volatile elements in multimetal-oxide films prepared by pulsed laser ablation
Jpn. J. Appl. Phys. Part 2 **35** (1996). (Accepted and now in press)

9) Atsushi Masuda, Ken-ichi Itoh, Minoru Kumeda and Tatsuo Shimizu
Origin of charged dangling bonds in nitrogen-doped hydrogenated amorphous silicon
J. Non-Cryst. Solids (1996). (Accepted and now in press)

10) Haruo Yokomichi, Atsushi Masuda, Yasuto Yonezawa and Tatsuo Shimizu
N_2-plasma-nitridation effects on porous silicon
Thin Solid Films (1996). (Accepted and now in press)